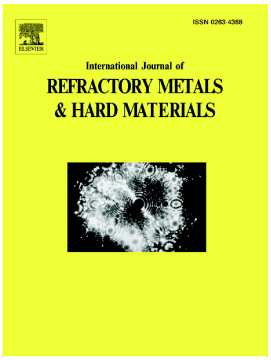

Additive manufacturing of tantalum scaffolds: Processing, microstructure and process-induced defects

Abdul Azeez Abdu Aliyu, Kitti Poungsiri, Junji Shinjo, Chinnapat Panwisawas, Roger C. Reed, Chedtha Puncreobutr, Krittima Tumkanon, Surasak Kuimalee, Boonrat Lohwongwatana

PII: S0263-4368(23)00032-X

DOI: https://doi.org/10.1016/j.ijrmhm.2023.106132

Reference: RMHM 106132

To appear in: *International Journal of Refractory Metals and Hard Materials*

Received date: 1 November 2022

Revised date: 19 January 2023

Accepted date: 23 January 2023

Please cite this article as: A.A.A. Aliyu, K. Poungsiri, J. Shinjo, et al., Additive manufacturing of tantalum scaffolds: Processing, microstructure and process-induced defects, *International Journal of Refractory Metals and Hard Materials* (2023), https://doi.org/10.1016/j.ijrmhm.2023.106132

Additive Manufacturing of Tantalum Scaffolds: Processing, Microstructure and Process-induced Defects

Abdul Azeez Abdu Aliyu[a], Kitti Poungsiri[b], Junji Shinjo[c], Chinnapat Panwisawas[d], Roger C. Reed[e], Chedtha Puncreobutr[a], Krittima Tumkanon[a], Surasak Kuimalee[f] and Boonrat Lohwongwatana[ab]*,

[a]*M3D Laboratory, Advanced Materials Analysis Research Unit, Department of Metallurgical Engineering, Faculty of Engineering, Chulalongkorn University, Phayathai Road, Wangmai, Pathumwan District, Bangkok 10330, Thailand.*

[b]*Biomechanics Research Center, Meticuly Co. Ltd., Pathumwan, Wang-mai District, Bangkok, Thailand.*

[c]*Next Generation Tatara Co-Creation Centre (NEXTA), Shimane University, 1060, Nishikawatsu, Matsue 690-8504, Japan.*

[d]*School of Engineering and Materials Science, Queen Mary University of London, London E1 4NS, United Kingdom.*

[e]*Department of Materials, University of Oxford, Parks Road, Oxford, OX1 3PH, UK.*

[f]*Industrial Chemistry and Textile Technology Program, Faculty of Science, Maejo University, 50290 Chiang Mai, Thailand.*

*__Corresponding author__: Boonrat Lohwongwatana
Tel.: +66-2-218-6939 (office), Fax: +66-2-218-6942
e-mail: boonrat@gmail.com

Abstract: Extreme melting point, high density, and ease of oxidation of tantalum (Ta) make its processing rather difficult using conventional methods. Additive manufacturing (AM) serves as an alternative Ta processing technique with unique design flexibility, customization, and minimizing material wastage. However, most additively manufactured parts contain undesired microstructural features or deviations (process-induced defects). This study aimed to assess the processability of the solid and structurally porous scaffolds of Ta through laser powder-bed fusion (LPBF) AM. It will further characterize and evaluate microstructure of LPBF processed Ta, with emphasis on assessing the mechanism of the process-induced defects. The x-ray diffraction (XRD) and microstructural investigation confirmed the presence of BCC Ta phase containing columnar, equiaxed and fine grains with roughness between 3.88 nm to 10.40 nm. The presence of oxygen resulted in the formation of some oxide phases such as Ta_2O_5 and Ta_2O_3. Numerous process-induced defects, including solidification-induced micropores, pores-induced and solidification-induced microcracks were identified. The dislodge unmelted or partially fused Ta powder resulted in other form of defects including micro-concaves and microgrooves. The mechanism of pore formation during the LPBF of Ta was assessed through computational simulation and its findings rationalised the experimental results.

Keywords: Tantalum; Additive Manufacturing; Defects; Microstructure; Implant; Laser powder-bed fusion

1 Introduction

Owing to their high strength, high ductility, resistance to corrosion and biocompatibility behaviour, refractory metals becomes widely used as biomaterials for the fabrication of medical devices, orthopaedic or load-bearing implants [1]. Tantalum (Ta) was first discovered by Anders Gustaf Ekeberg of Sweden in 1802 and its clinical application as biomaterial can be traced back to 1940s [2, 3]. Robertson and Peacher [4] utilize Ta medical devices in the form of plate, foil, wire and ribbon to accurately perform the nerve suture, repair cranial defects, inhibits postoperative adhesions and secure hemostasis without adverse effect to the surrounding tissues. Various *in-vivo* and *in-vitro* studies confirmed the excellent osteointegration, exceptional biocompatibility, high strength and good corrosion resistance of Ta implant [5-7]. Another study by Matsuno, et al. [8] further confirmed the non-toxicity and biocompatibility of the Ta. Compared to the most commonly used surgical grade biomaterial like Ti-6Al-4V, the adhesion, proliferation and differentiation of human osteoblast cells was remarkably observed on the Ta surface [9]. Meijer, et al. [10] investigated the strain distribution and stability of the tibial plateau reconstruction using Ta trabecular cones. The implant was found to have high stability with good strain distribution. Despite the outstanding biological performance and numerous advantages of Ta over the currently used metallic biomaterials, its application as biomaterial is limited, especially for making large implants owing to its high density and high cost [11]. In early 2000s, the surge in research related to Ta porous implants was noticed after the introduction of porous Ta acetabular cup implants by Trabecular Metal^{TM} (Zimmer, Warsaw, IN, USA). However, processing of both solid and porous Ta is challenging through conventional techniques such as lost wax casting, furnace sintering and electron beam melting, owing to its extreme melting point (2996 ^{o}C), high density (16.68 g/cm^{3}) and high affinity to oxygen [12, 13].

In recent years, there is rising attempts to fabricate both solid and porous Ta implants through additive manufacturing (AM), specifically laser powder-bed fusion (LPBF) [14-19]. LPBF utilized computer-aided design (CAD) to build a part through layer-by-layer powder deposition following the prescribed laser scan path [20, 21]. The advantages of LPBF include its freedom to design porosities and macro/microstructures of the implants, which allow control of mechanical properties, fabrication of complex structures to match that of human bone and to enable patient-specific implants [17, 22, 23]. Chandhanayingyong, et al. [24] utilize LPBF to fabricate a highly complex and patient-specific proximal phalangeal prosthesis, whereby a giant cell tumor in the toe was successfully treated. In another study by Zhao, et al. [25], a porous scaffold of Ta was developed through gel casting-based 3D printing coupled with an electrolytic reduction. The fabricated scaffolds were found to have high strength (4.1 ± 0.4 MPa) close to that of cancellous bone (4–12 MPa) and facilitate the cells proliferation.

Although, researches on processing solid and porous Ta through LPBF approach could be found [26-29], there are still key issues which require an in-depth understanding and systematic investigation. An extremely high cooling rate coupled with non-equilibrium solidification during the LPBF of metals resulted in various process-induced defects [30, 31]. Gong, et al. [32] revealed the formation of other defects, including micro-concaves and microgrooves during LPBF of Ti-6Al-4V implant. These defects seriously degrade the mechanical and biomedical behaviours of metallic implants. However, to the best of the authors' knowledge, little has been focused on assessing the causes, distribution, occurrences and formation mechanisms of the process-induced defects that normally formed on the additively manufactured solid and porous Ta parts. Hence, these motivated the idea for this research.

In this study, solid and porous scaffolds of Ta were designed using ANSYS 2020r1 software and processed through LPBF technique. The fabricated specimens were characterized through

various characterisation methods which are field emission scanning electron microscopy (FESEM), optical microscopy (OM), energy dispersive x-ray spectroscopy (EDX), x-ray photoelectron spectroscopy (XPS) and x-ray diffraction (XRD). Microstructural investigation presents various deviations and undesired features resulting in LPBF process-induced defects. BCC Ta enriched with columnar, equiaxed and fine grains and some oxide phases like Ta_2O_3 and Ta_2O_5 was identified. A numerical simulation demonstrating the pores generation and formation mechanism during the LPBF of solid and porous scaffolds of Ta is also presented.

2 Method

2.1 Design of solid and porous scaffolds of Ta

ANSYS 2020r1 software was employed to design and model the solid and the porous scaffolds of Ta specimens. The compute-aided design (CAD) models are then saved in STereoLithography (STL) file, and the redesigned models were imported in the form of STL format files. Different sizes of the cubic solid Ta specimens namely D-Ta1, D-Ta2 and D-T3 with dimensions 5 mm, 10 mm and 15 mm, respectively were designed. The purpose of the solid specimens is to allow comparison with the porous specimens. Octet truss and diamond truss with dimensions 10 × 10 × 12 mm with 25 % and 50 % infill density were used for the porous scaffolds. Various designs of the porous scaffold of Ta specimens were levelled S-Ta1, S-Ta2, S-Ta3 and S-Ta4 as indicated in Figure 1.

Name	Unit cells	Porous scaffolds Pore size

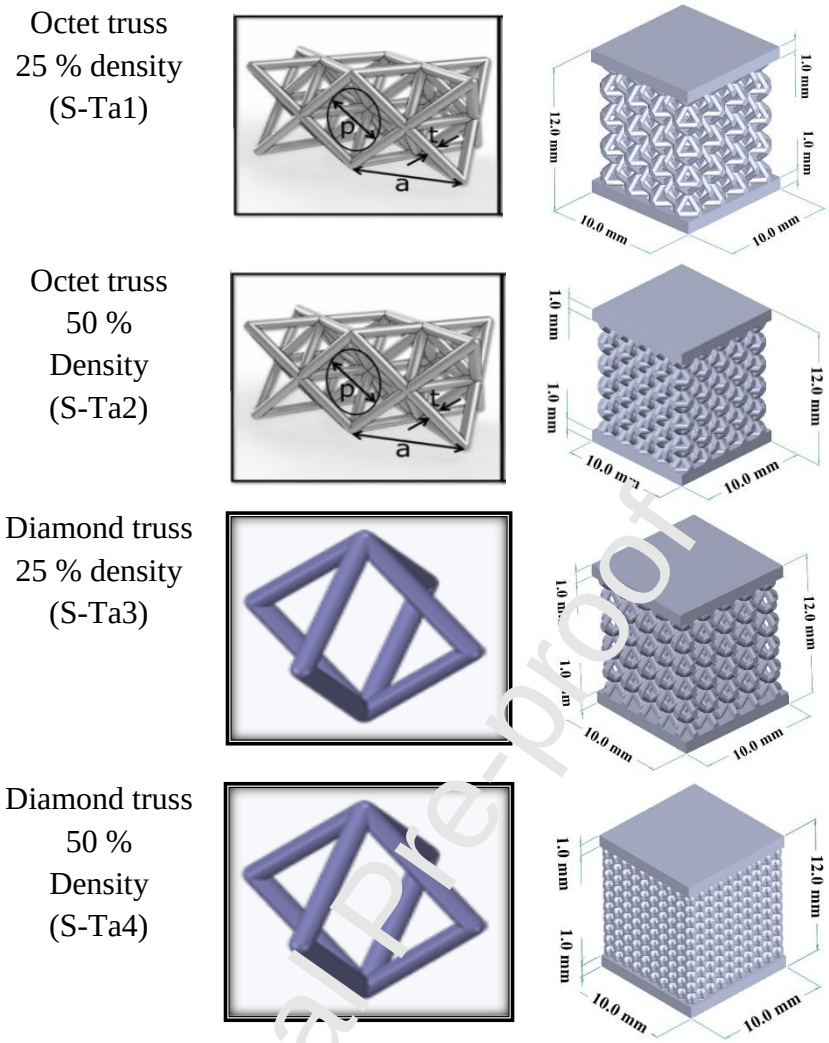

Figure 1 Computer-aided design of the unit cells and the porous scaffolds with respective pores density.

2.2 LPBF of solid and porous scaffolds

Both solid and porous scaffolds of Ta were 3D printed based on the CAD models using LPBF equipment (FARSOON Technologies Inc. and MiCap Machinery co. ltd., Changsha, Hunan, China). A medical grade pure Ta powder, which is also supplied by FARSOON Technology, China with physical properties shown in Table 1 is used to fabricate the solid and the porous scaffold specimens. The 3D printed specimens were dried for 90 mins at an ambient temperature after printing. Trapped and unbounded powder was removed by a compressed air and ultrasonic washing. Bulk porous part is built by selectively melting the powder through the laser beam and the subsequent layer is formed by spreading the powder on the previous layer

consecutively. The process continues until the designed bulk Ta part is formed. The manufacturing process of the specimens was throughout conducted in a vacuum shield with an Argon atmosphere to avoid oxidation. The infill and the borderline parameter conditions used for processing Ta specimens through LPBF process are presented in Table 2.

Table 1 Physical properties of Pure Tantalum powder (source: manufacturer's Data)

Physical properties	Value	Unit
Density	≥16.360	g/cm^3
Yield Strength	Rp0.2≥140	MPa
Tensile strength	Rm≥210	MPa
Compressive strength	≥15	MPa
Bending strength	≥700	MPa
Elongation	A≥27	%
Hardness	≥100	HV10

Table 2 Different operating parameter between infill and borderline

Operation parameter	Infill parameter	Borderline parameter
Layer thickness	0.03 mm	0.03 mm
Laser power	250 W	100 W
Scanning speed	100 mm/s	500 mm/s
Laser wavelength	1060 nm	1060 nm
Laser spot size	85 μm	128 μm

The laser energy used in this study can be estimated via Equation 1.

$$\text{Laser energy (E)} = \frac{\text{P (W)}}{\text{v (mm/s)} \times \text{t (mm)} \times \text{h (mm)}} \quad (1)$$

where P is the laser power, v is the scanning speed, t is the layer thickness and h is the hatch spacing [33]. Using the infill and borderline parameter settings (Table 2), the laser energy was computed to be 83.3 J/mm^3 and 6.7 J/mm^3 for the infill and borderline parameters, respectively.

2.3 Dimensional accuracy and relative density

To determine the dimensional accuracy of the LPBF processed solid and porous scaffolds of Ta, each side of the specimens was measured using vernier calliper. The measurement was repeated five times and the average value was calculated. To estimate the errors between the measured and design values, standard deviation was computed. Density and relative density were determined using the displacement method according to ASTM D792 standard [34]. The mass of the fabricated solid Ta specimens was weighed in air. It was then immersed in deionised water (DI) and the apparent mass of the specimen is determined. Then the density and the relative density (specific gravity) of the specimens were calculated using Equations 2 and 3, respectively.

$$\text{Density} = \frac{w_a}{w_a - w_w} \tag{2}$$

$$\text{Relative density} = \frac{\rho_{substance}}{\rho_{reference}} \tag{3}$$

where:

w_a = apperent mass of specimen in air

w_w = apparent mass of totally immersed spacimen in water

$\rho_{substance}$ = density of the substance been measured,

$\rho_{reference}$ = density of the reference

2.4 Metallographic specimen preparation for microstructural investigation

Solid and porous 3D printed Ta specimens were prepared through four stages to enable microstructural observations as prescribed by the standard metallographic procedures. Firstly,

the specimens were cut perpendicular to the direction of scan. In the second stage, the specimens were mounted to enable proper handling and safe grinding. The next stage involved grinding using premium grade abrasive paper (93U-4854) and polishing by 1 µm water-based diamond suspension through a conventional grinding/polishing technique. Last stage involved etching of the specimens using 50 % lactic acid, 30 % sulfuric acid and 20 % hydrochloric acid etchants solution for 2 min at room temperature.

2.5 Characterization

Field emission Scanning electron microscopy (FESEM, FEI Quanta FEG 250, Thermo Fisher Scientific, Hillsboro, OR, USA) at 15 kV and optical microscope (OM, Hubitz - HRM 300, Korea) were used to visualise and analyse the microstructure and the microstructural defects in the LPBF-processed solid and porous Ta specimens. Further analysis to assess the pore shape, size and the area density through Image J (KEYENCE VR3000, Japan) analysis was performed. The surface topology and roughness were evaluated using atomic force microscope (AFM, Veeco, Dimension 3100, Plainview, NY, USA). The chemical compositions and phases of the LPBF processed solid and porous scaffold of Ta were analysed through energy dispersive x-ray spectroscopy (FEI Quanta FEG 250, Thermo Fisher Scientific, Hillsboro, OR, USA), x-ray photoelectron spectroscopy (XPS, Bara Scientific Co., Ltd., series Axis Ultra) and x-ray diffraction (XRD, Bruker D8 Discover). The XRD measurement was carried out at step size 0.01° and scanning range of $2\theta = 10°$ to 90° using CuKα radiation at 15kV, 30 mA.

2.6 Thermal-fluid flow during LPBF AM

A computational fluid dynamics (CFD) calculation is used to investigate the thermal-fluid flow dynamics of the melt pool to understand porosity development and surface structure to

rationalise the microstructure observation from experiment. Our in-house CFD code called TATM-MEX has been adopted to model the interaction between the laser heat source and the powder materials [35]. The governing equations for fluid flow dynamics are presented in equations 4.1, 4.2 and 4.3:

$$\frac{\partial \rho}{\partial t} + (\mathbf{u} \cdot \nabla)\rho = -\rho \nabla \cdot \mathbf{u} \tag{4.1}$$

$$\frac{\partial \mathbf{u}}{\partial t} + (\mathbf{u} \cdot \nabla)\mathbf{u} = -\frac{\nabla p}{\rho} + \mathbf{Q_u} + \mathbf{g} + \mathbf{F}_{\mathbf{u},surf} \tag{4.2}$$

$$\frac{\partial T}{\partial t} + (\mathbf{u} \cdot \nabla)T = -\frac{p \nabla \cdot \mathbf{u}}{\rho c_p} + Q_T + \frac{1}{\rho c_p} q_L \tag{4.3}$$

Here, $\mathbf{Q_u}$ is the viscous term and $\mathbf{g}$ is the gravitational acceleration. All the interfacial phenomena present within the LPBF process, including surface tension, Marangoni's flow (thermo-capillary force) and recoil pressure have been incorporated in the simulation as $\mathbf{F}_{\mathbf{u},surf}$ as adopted by [35]. The liquid/gas interface is captured by the level-set method, combined with the volume-of-fluid method to ensure volume conservation. The laser heat source q_L is calculated by tracking light propagation using the ray-tracing method, and the heat loss due to vaporisation, conduction, convection and radiation have also been considered in Q_T. Details of Modelling description can be found elsewhere [35]. The physical properties of tantalum used in the simulation are summarised in Table 3.

Table 3 Thermo-physical properties of Ta [35]

Thermo-physical properties	**Value**	**Unit**
Atomic weight	180.95	g/mol
Solid density	16654	kg/m^3
Liquid density	15000	kg/m^3
Melting temperature	3258	K
Boiling temperature	5783	K

Δh_{melt}	36.6	kJ/mol
Δh_{boil}	733	kJ/mol
Surface tension, σ_0	2150	mN/m
Surface tension gradient, $\frac{d\sigma}{dT}$	-0.21	mN/m/K
Viscosity, μ	$\mu(T) = 0.0035 \exp(213.3 \times 10^3/RT)$	mPa·s
Heat capacity at melting temperature, c_p	41.8	J/mol/K
Thermal conductivity at melting temperature, λ	47	W/m/K

2.7 Vickers hardness

The microhardness of the LPBF processed solid and porous scaffolds of Ta was determined according to standard test method provided by ASTM E98-82. The test was carried out using Vickers hardness testing machine (ZWICK, mode: 3214) and indented via diamond indenter. The load of 0.5 kg was applied at a slowdown speed and dwell time of 15 seconds. For each specimen, the hardness measurement was carried out five times at different locations and average value was recorded.

3 Results

3.1 LPBF processing of solid and porous tantalum

Unlike conventional processes, Wauthlé, et al. [36] showed that, fully dense Ta components can be processed through LPBF technique with satisfactory mechanical properties as required by ISO 13782 of the pure Ta for surgical applications. Different sizes of the solid and porous Ta scaffolds were fabricated through LPBF technique (Figure 2). The dimensional accuracy was measured in x, y and z-directions as presented in Figure 2a-c and the results shown in Table 4. The percentage dimensional deviation (error) observed in the D-Ta1, D-Ta2 and D-Ta3 Ta specimens are 1.13 %, 1.10 % and 0.55 %, respectively. The relative density of each solid Ta specimen measured through Archimedes method is presented in Table 5. The solid Ta specimens D-Ta1, D-Ta2 and D-Ta3 were found to have a very high relative density of 99.56

%, 98.99 % and 99.43 %, respectively. The specimen D-Ta2 has the lowest relative density. Therefore, it is selected for the subsequent pore analysis.

Table 4 Dimensional accuracy of D-Ta1, D-Ta2 and D-Ta3 Ta specimens

Directions	**D-Ta1**		**D-Ta2**		**D-Ta3**	
	Design (mm)	Measured/Std. dev. (mm)	Design (mm)	Measured/Std. dev. (mm)	Design (mm)	Measured/Std. dev. (mm)
X	5.0	5.1±0	10.0	10.18± 0.02	15.0	15.12± 0.08
Y	5.0	5.1±0	10.0	10.15± 0.04	15.0	15.13± 0.05
Z	5.0	5.0±0	10.0	10.0±0	15.0	15.0±0

Table 5 Average measured density and relative density of the solid Ta specimens

Density	AVG (g/cm^3)	Relative density (%)
D-Ta1	16.58 ± 0.11	99.56
D-Ta2	16.56 ± 0.02	99.99
D-Ta3	16.66 ± 0.01	99.43

Porous scaffolds of Ta were designed and fabricated through LPBF technique (Figure 2d-g). The designed pore and strut of Ta scaffolds were printed using the imported CAD model in the form of STL files. The 25 % and 50 % infill density were designed for both diamond and octet truss scaffolds. The actual strut thickness of the scaffolds was compared with the average thickness of the measured values.

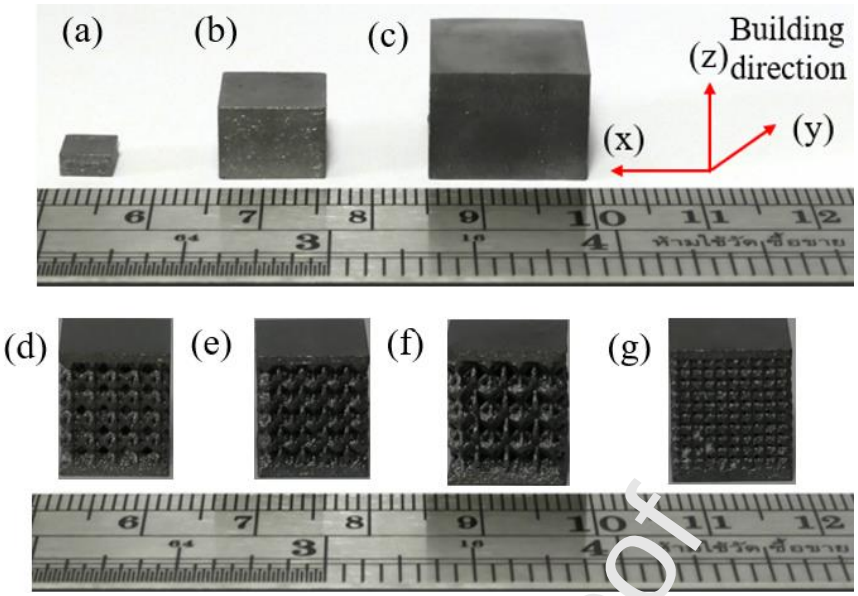

Figure 2 LPBF processed solid and porous Ta specimens with direction of measurements and dimensions (a) D-Ta1 (b) D-Ta2 (c) D-Ta3 (d) S-Ta1 (e) S-Ta2 (f) S-Ta3) (g) S-Ta4.

The optical microscope images were used to measure and determine the strut thickness of the LPBF processed porous scaffolds of Ta (Figure 3). Three strut thickness values at different locations along the strut length was measured and average values were computed. To determine the mismatch between the designed and the 3D printed scaffolds of Ta, the standard deviation was calculated as indicated by the error bar (Figure 4). The highest discrepancy of 34.66 µm is observed in the S-Ta3 specimen. The strut thickness was designed as 465.0 µm while the measured thickness was found to be 511.26 µm. The smallest discrepancy of 7.89 µm was found in the S-Ta2 specimen.

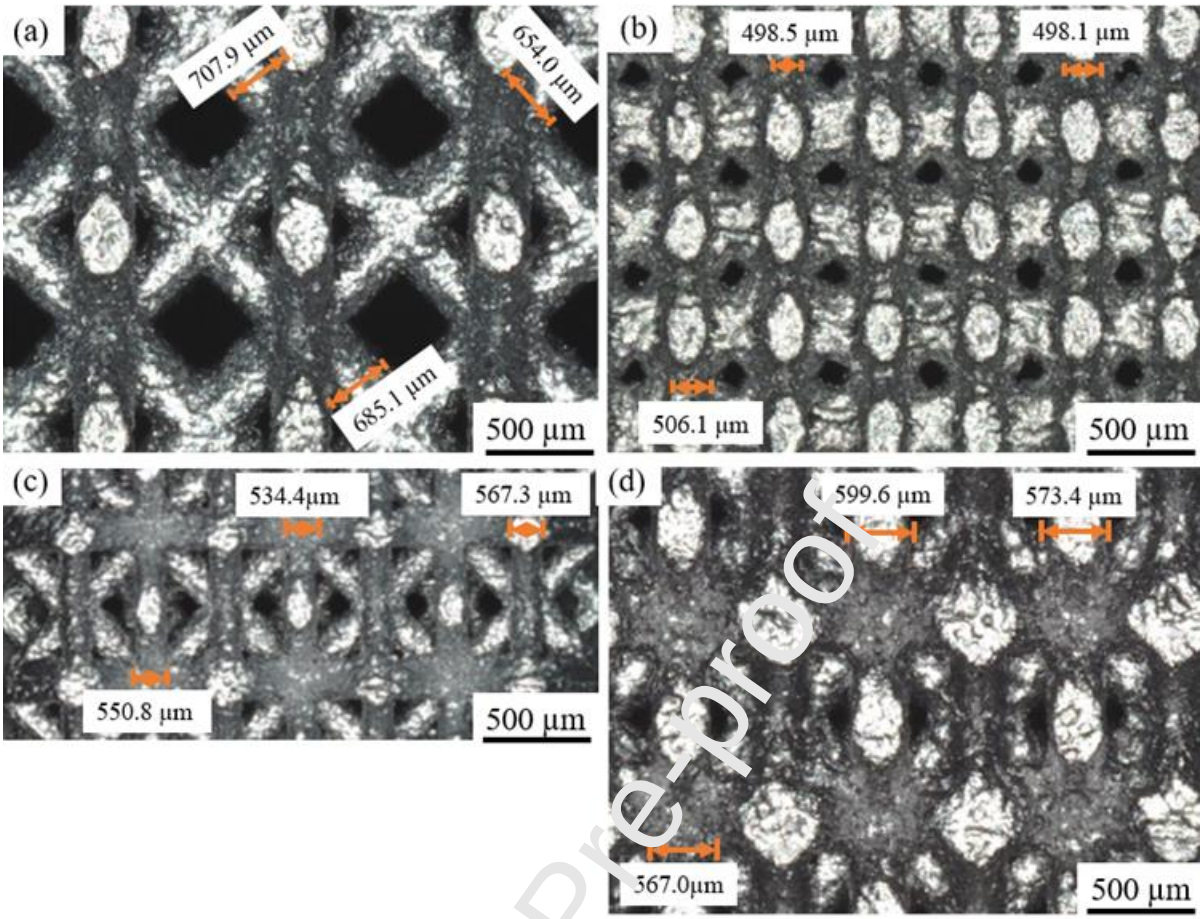

Figure 3 Optical micrographs comparing the mismatch between the LPBF-processed porous scaffolds of Ta, indicating the measured struts thickness (a) S-Ta1 (b) S-Ta2 (c) S-Ta3 and (d) S-Ta4 specimens.

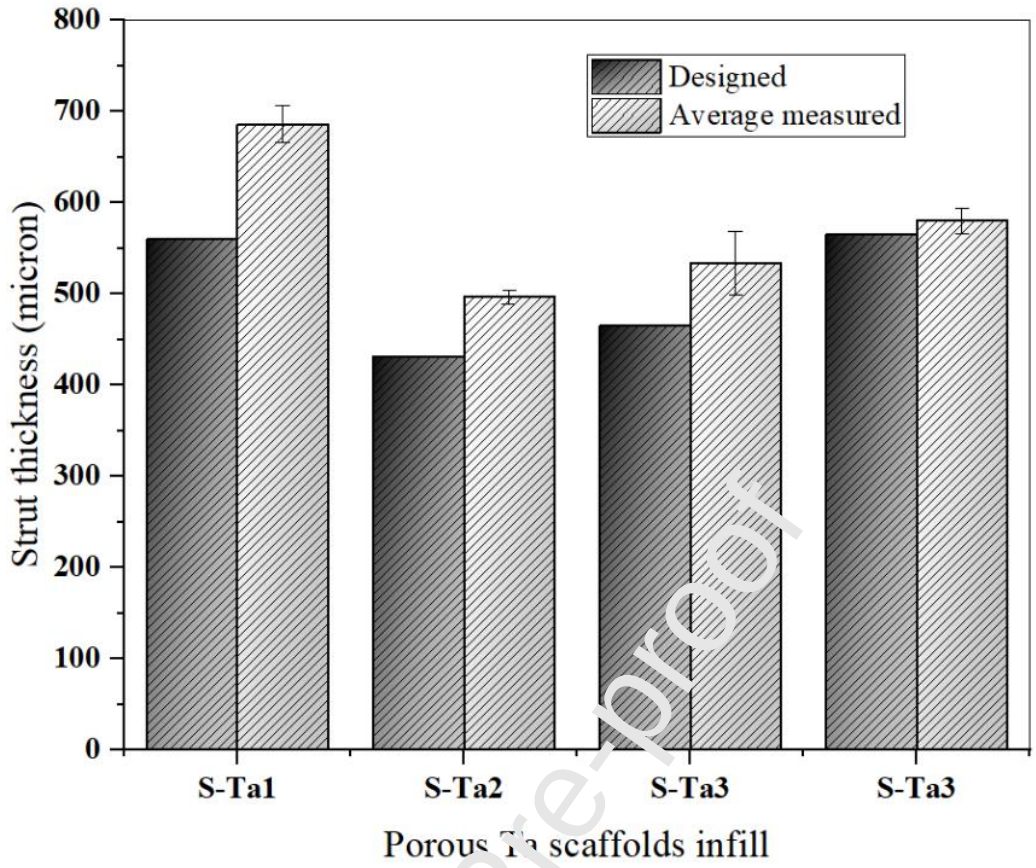

Figure 4 Design versus average measured strut thickness of the S-Ta1, S-Ta2, S-Ta3, S-Ta4 specimens processed through LPBF indicating the error bar of the measured strut thickness.

3.2 Chemical composition and phase analysis

The EDX, XPS and XRD characterization tools were utilized to assess chemical compositions of the LPBF-processed Ta specimens. Very long peak and numerous short peaks of Ta were observed in the EDX spectrum shown in Figure 5a. Despite the presence of a very short oxygen peak (Figure 5b), Ta dominates the LPBF processed solid specimens. Being an oxygen getter, it is quite tedious to separate oxygen from Ta powder. Therefore, 0.5 % and 0.6 % of oxygen was detected by the EDX analysis in the fabricated Ta specimens at different locations, Figure 5a and Figure 5b, respectively. Oxygen is believed to infiltrate the Ta powder during passivation for LPBF processing or more likely from the metallurgical preparation. It is beneficial to the implants by reacting with the alloying elements to form biocompatible metallic oxides. Another benefit of oxygen in metallic alloy is its hardening capability, which enhance

the hardness of the processed part. The elemental mapping for Ta and O, which shows the distribution of both elements in the built Ta parts is presented in Figure 5c and Figure 5d, respectively.

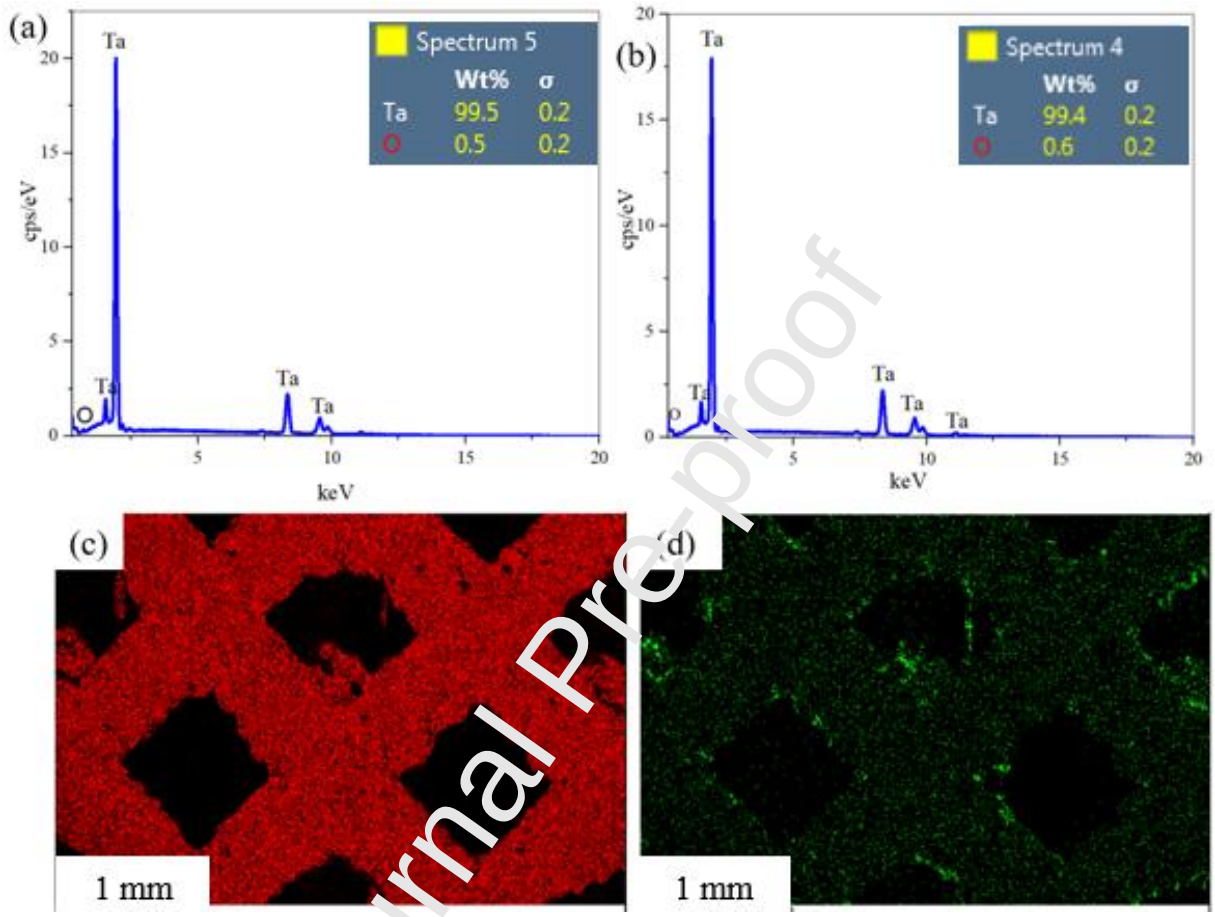

Figure 5 SEM-EDX spectrum of the porous Ta specimen (S-Ta1) (a) numerous long peaks and short peaks of tantalum and oxygen, containing about 99.5 % and 0.5 %, respectively (b) 99.6 % Ta and 0.4 % (c) elemental mapping showing the distribution of tantalum and (c) oxygen.

Figure 6 shows the XPS spectra of the LPBF processed Ta. The chemical states and the oxide species are shown in Figure 6a. The presence of oxygen in the LPBF processed specimen is further confirmed by the observed O1s XPS spectra (Figure 6b). The O1s spectrum contained two regions of Ta_2O_3 and Ta_2O_5 oxide compounds with a binding energy of 531.5 eV and 532.8 eV, respectively. The Ta4f spectrum shown in Figure 6c also contains two regions of Ta4f2/5

and Ta4f7/2 at a binding energy of 27.5 eV and 29.5 eV, respectively. These two species of Ta4f are believed to be responsible for the formation of metallic oxides.

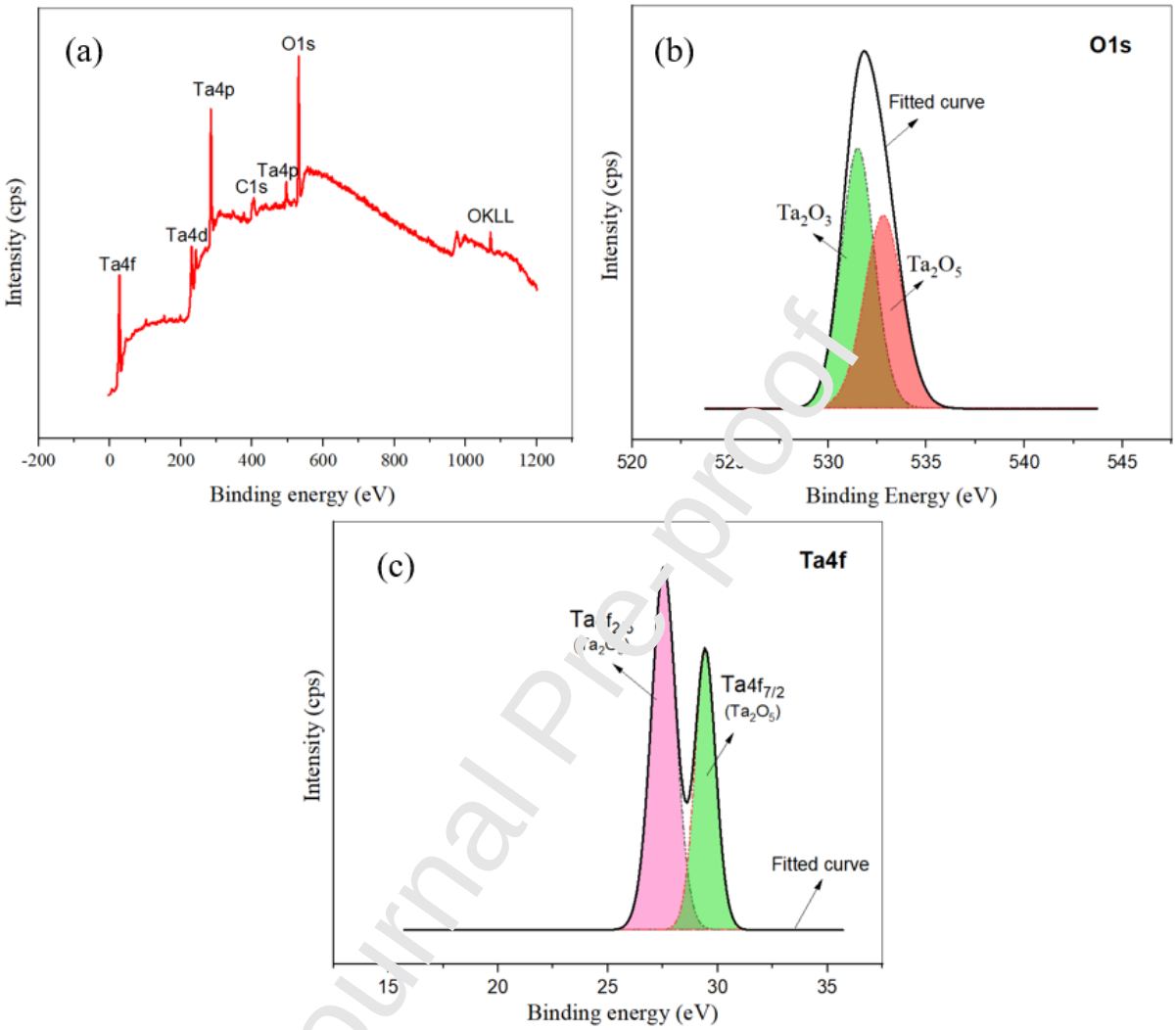

Figure 6 XPS spectra of LPBF processed Ta indicating the chemical compositions and oxide species (a) chemical states of Ta (b) O1s spectrum (c) Ta4f spectrum.

The XRD patterns of the LPBF-processed solid and porous Ta processed at low and high energy conditions is presented in Figure 7. It revealed similar diffraction patterns in most of the specimens and parameter settings, which contained highly BCC Ta phase. The long sharp Ta peaks observed at 2θ = 38°, 57°, 70° and 83° confirmed the crystalline nature of the LPBF processed solid and porous scaffolds of Ta (Figure 7a). Despite Ar protection during sintering, other secondary peaks of Ta_2O_5 precursor were detected at 2θ = 45°, 65° and 78°. This is

believed to occur due to reaction of Ta with O, which previously detected by the EDX and XPS analysis. However, no secondary peaks of Ta_2O_5 or metallic oxide were observed in the D-Ta2 specimen. This further confirmed that, the oxygen is not present in the feedstock, rather infiltrated the LPBF processed Ta during the postprocessing. The diffraction peaks of BCC Ta phase in the porous Ta scaffolds (S-Ta1-4) are longer and broader than those of solid Ta (D-Ta1-3) as seen in Figure 7b. This might relate to the formation of highly refined microstructures and hence, enhanced residual stresses [23].

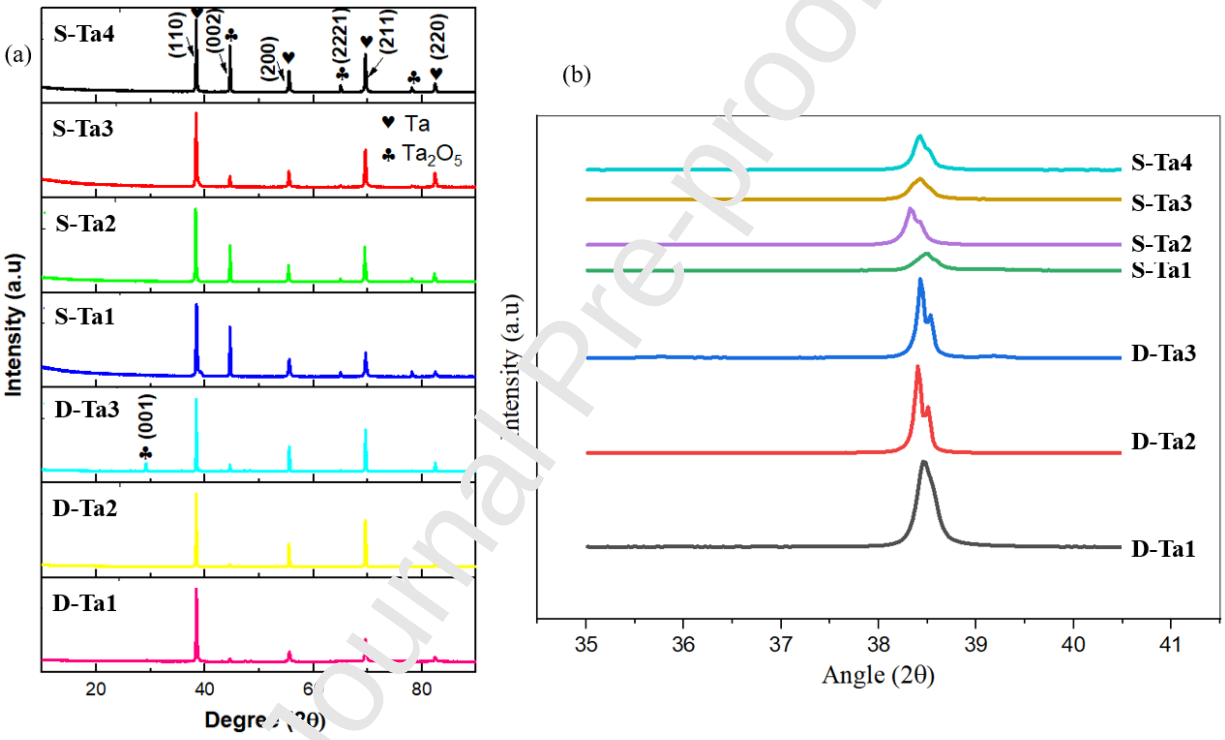

Figure 7 XRD spectrum of LPBF processed solid and porous Ta specimens (a) various peaks of Ta and Ta_2O_5 phases (b) Ta peaks within $2\theta = 35^o$ and 45^o presenting the broadness of the peaks.

3.3 Topography and microstructural evaluation

SEM micrograph revealing the microstructure of the LPBF-processed Ta scaffold (S-Ta1) at borderline parameter settings is displayed in Figure 8. The micro-concaves observed in Figure 8a are believed to be resulted from dislodged Ta particles during the conventional

grinding/polishing processes. Large columnar grains, which believed to be grown along the building direction were observed (Figure 8b). Thermal gradient along the solid/liquid interface in the pool boundaries, which normally occurred during LPBF process resulted in columnar grains growth along the building direction [37]. Equiaxial grains and fine nano structures were also observed (Figure 8c and e). These nano-structural features enhance not only the ductility or mechanical properties of the LPBF processed part, but also its biological properties such as cell adhesion and proliferation.

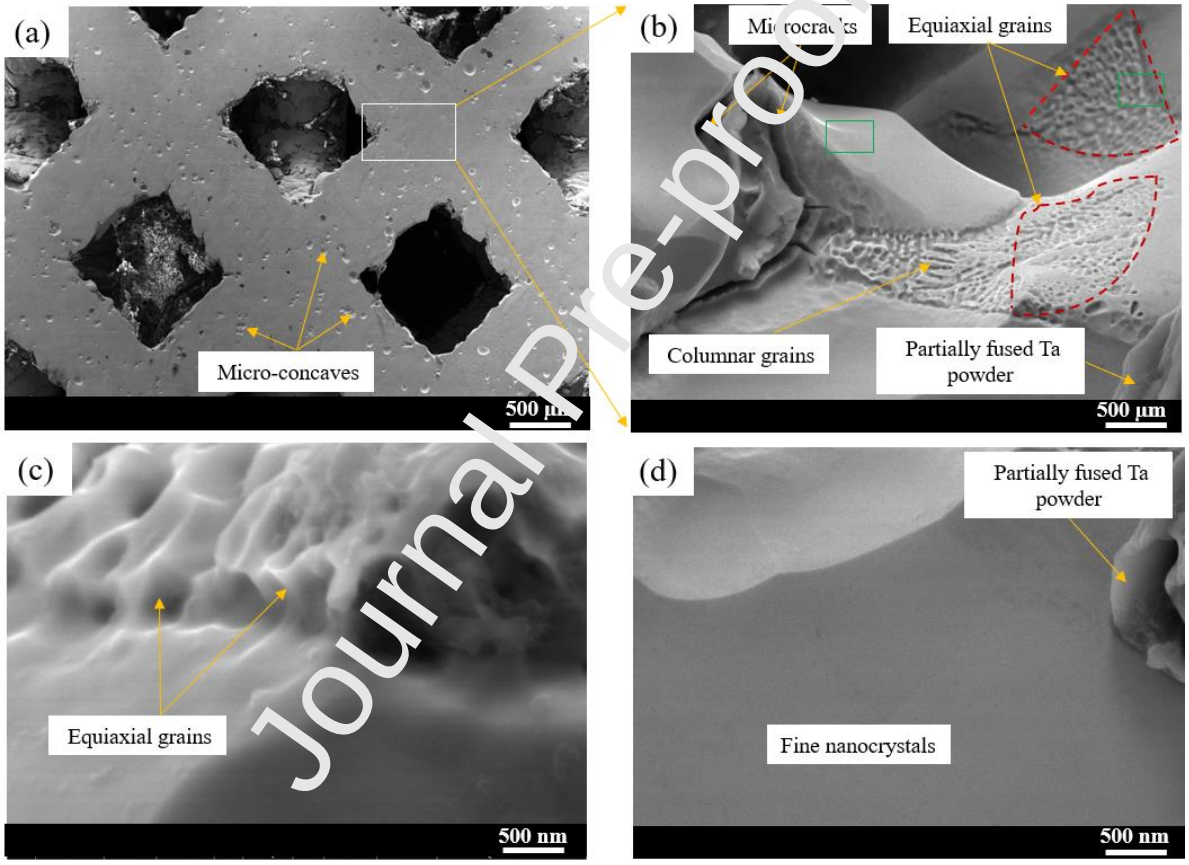

Figure 8 FESEM micrographs of LPBF processed S-Ta1 specimen revealing (a) microstructure with various micro-concaves due to dislodged partially fuse Ta powder (b) columnar and equiaxial grains, solidification-induced microcracks and the partially fused Ta powder (c) equiaxial grains (d) fine grains.

The presence of nano-structural features on the LPBF-processed Ta surface was further analysed through AFM (Figure 9). The 3D surface topography analysed over an area 20 µm x

20 µm revealed various uniform sharp peaks, indicating the nanostructured surface of the LPBF-processed Ta. The peak intensity of D-Ta1 is longer and hence, has a high average surface roughness of 10.40 nm (Figure 9a). To better understand the level of the roughness intensity, the pattern is presented (Figure 9b). The relatively low roughness of 5.09 nm and 3.88 nm was recorded for D-Ta2 (Figure 9c) and D-Ta3 (Figure 9d), respectively. Thus, the roughness decreases with an increase in the specimen size. This could occur due to two reasons: Firstly, an increase in unmelted or partially fused Ta powder with decrease in LPBF-processed Ta specimen size. Dislodging the partially fused Ta powder increase the surface roughness resulted in deeper concavity and microgrooves, hence, higher roughness. Secondly, increase in residual stress accumulation with a decrease in the specimen size, which increase the grain coarsening, hence, increase the surface roughness.

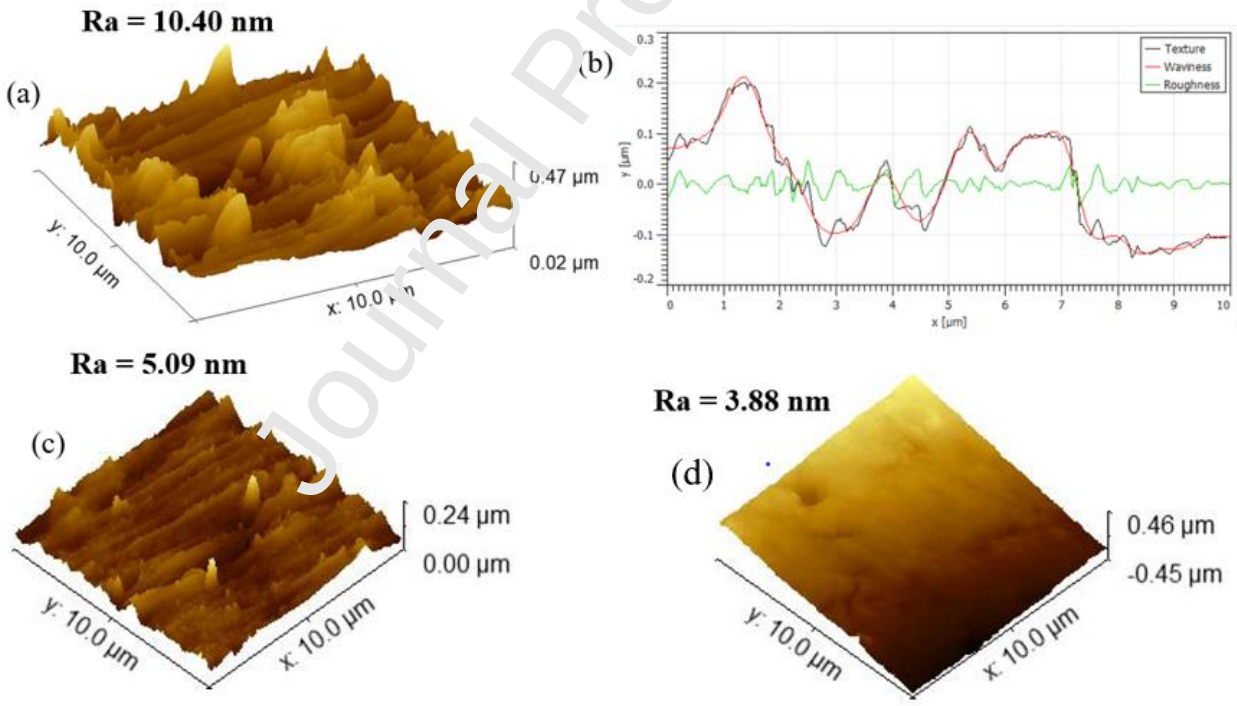

Figure 9 AFM images showing the surface topology and roughness of LPBF-processed solid Ta (a) D-Ta1 (b) D-Ta1 roughness profile (c) D-Ta2 (d) D-Ta3.

To further understand the microstructure of the LBBF-processed scaffold of Ta, the FESEM measurement of specimen S-Ta4 was presented in Figure 10. It revealed numerous partially

fused and unmelted Ta powder on the strut edges (Figure 10a). The spherical shape Ta particles on the LPBF processed part confirmed the presence of unmelted Ta powder, which bonded together to form microgrooves (Figure 10b). This confirmed the inability of the LPBF process to completely melt the Ta powder, which might relate to an extremely high melting temperature property of the Ta powder [38]. Further investigation at high magnification revealed some partially fused Ta particles on the scaffold surface as depicted in Figure 10c. The unmelted and partially fused Ta particle was removed through conventional grinding/polishing processes. However, it resulted in the formation of some micro features such micro-concaves and microgrooves, as well as exposing the pores-induced microcracks (Figure 10d).

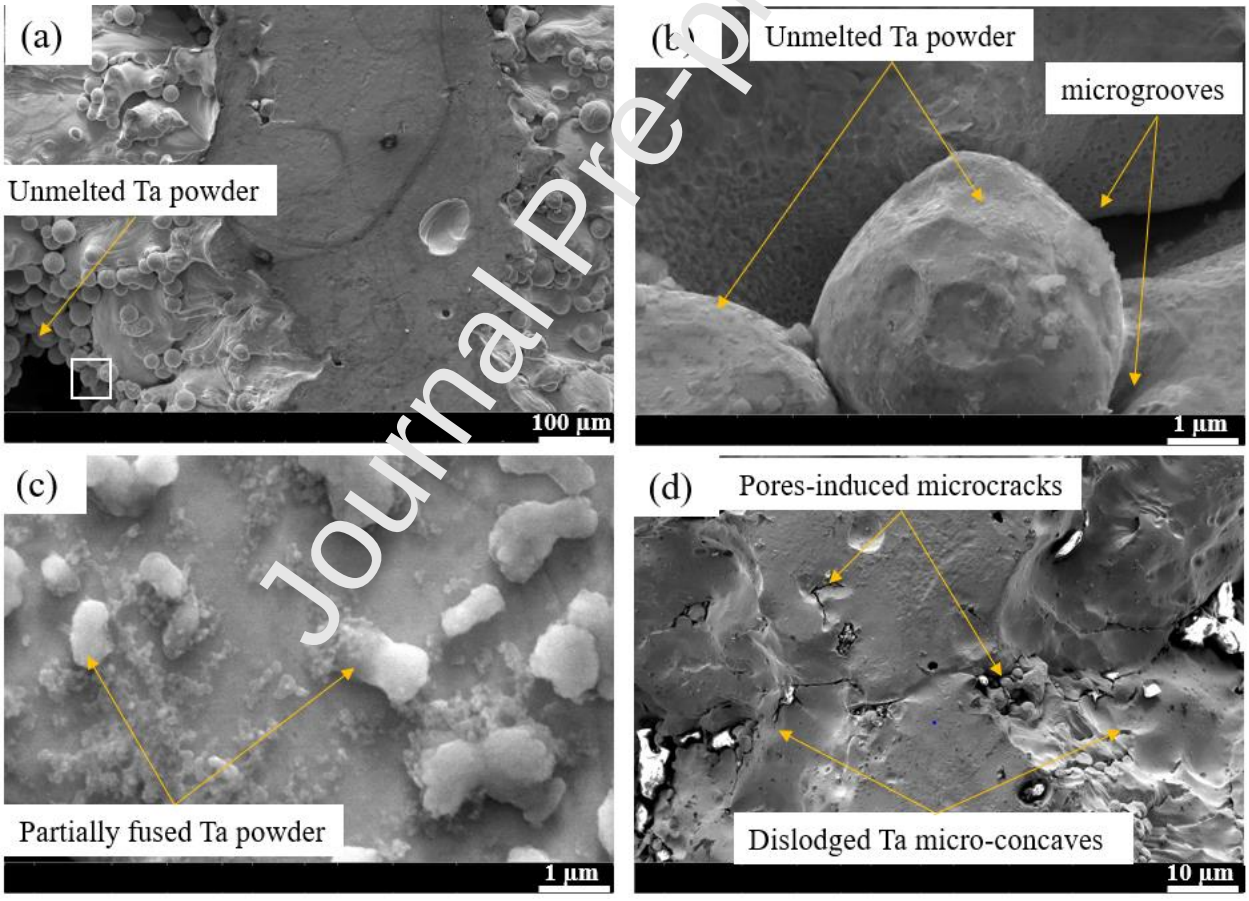

Figure 10 FESEM images of LPBF processed S-Ta4 specimen (a) various unmelted and partially fused Ta powder (b) higher magnification revealing the shape of the unmelted Ta powder and microgroove formation (c) partially fused Ta powder on the strut surface (d) pores-induced microcracks and micro-concaves due to dislodged unmelted Ta powder.

3.4 Process-induced defects evaluation

During the LPBF process, numerous undesired microstructural features or deviation, herein; referred to as process-induced defects are normally formed. These defects are detrimental to the quality and performance of the fabricated parts. In this study about five process-induced defects were identified. These include (i) pores-induced microcracks, which induced by interconnected micropores (ii) solidification-induced microcracks, which is formed due to shrinkage of the Ta molten pool during solidification (iii) solidification-induced micropores, which resulted from gasses vaporization during solidification of the molten pool (iv) micro-concaves and (v) microgrooves, which are formed due to dislodged unmelted or partially fused Ta powder. In this study, SEM images of the solid and porous scaffolds of Ta were employed to evaluate the process-induced defects that formed during LPBF process.

3.4.1 Solidification-induced micropores in solid Ta

Generally, process-induced micropores are formed on the LPBF-processed metallic parts due to low laser energy, which resulted in an incomplete melting and the vaporisation of the trapped gasses in the melt pool. However, when the energy is too high, melt instability occurred and the pores are formed due to solidification, herein referred solidification-induced micropores [39]. Solid LPBF-processed Ta (D-Ta2) was selected for the porosity analysis. The specimen was fabricated via the laser power of 250 W and scanning speed of 100 mm/s parameter conditions (high laser energy, E = 83.3 J/mm^3). Particle analyser command in ImageJ was used to examine the area porosity. Thresholding was used to select the features of the image and the number of the red pixels was measured (Figure 11a). The outline of the pores detected during the analysis is presented in Figure 11b. The measured percentage area porosity was found to be 1.19 %.

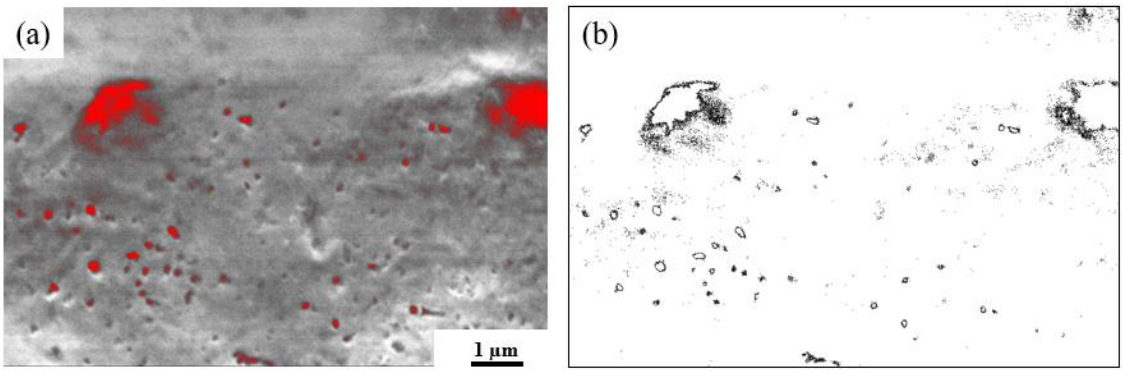

Figure 11 ImageJ pores analysis of the LPBF processed D-Ta2 specimen fabricated using high energy settings (a) normal to building direction (b) outline of the pores detected at surface area analysis.

The surface morphology of LPBF processed solid Ta specimens using 100 W and 500 mm/s power and scanning speed, respectively was presented in Figure 12. Despite low energy setting used, no clear process-induced defects observed in D-Ta1 specimen (Figure 12a). This is expected, owing to its high density of 99.56 %. A cluster of solidification-induced micropores (encircled in red) and highly rough surface was observed in D-Ta2 specimen (Figure 12b), which further observed through high magnification (Figure 12c). This may relate to its low density (98.99 %). The high roughness observed is due to lower laser energy (E = 6.7 J/mm^3) used, which is not sufficient to melt the Ta powder completely, owing to its extremely high melting temperature. Thus, the dislodged unmelted and partially fused Ta resulted in the deeper and narrow craters, hence the formation of rougher surface. Dramatic decrease in the micropores and smoother surface was noticed on the D-Ta3 specimen (Figure 12d). The decrease in solidification-induced micropores and improved roughness might also relate to the size of specimen. A similar finding was reported by Livescu, et al. [28], whereby less micropores was observed in a small size Ta specimen with less layer thickness.

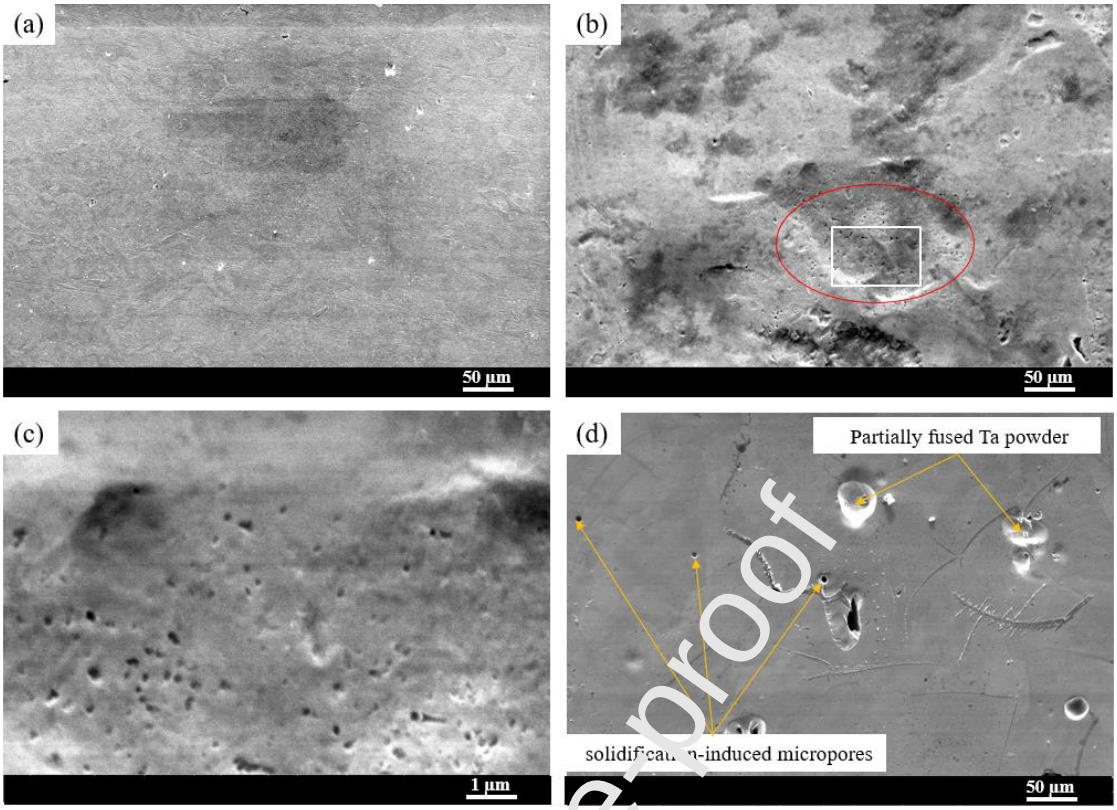

Figure 12 FESEM micrographs of LPBF processed solid Ta specimens presenting various solidification-induced micropores (a) D-Ta1 (b) D-Ta2, cluster of solidification-induced micropores encircled in red (c) D-Ta 3 observed at high magnification to clearly view the solidification-induced micropores (c) D-Ta 3 revealing the solidification-induced defects and partially fused Ta powder.

3.4.2 Process-induced defects in octet truss scaffolds

Figure 13 shows FESEM images of 50 % Octet truss porous scaffold of Ta (S-Ta2) processed through the power (250 W) and scanning speed (100 mm/s) parameter settings. It is obvious that various process-induced defects are present on the LPBF-processed surface (Figure 13a). The high energy density used in processing this specimen resulted to some shallow microgrooves and few pores-induced microcracks (Figure 13b). These defects are normally formed on the LPBF-processed surface due to dislodge unmelted or partially fused Ta powder.

The defects are not pronounced due to significant melting of Ta powder. However, it is accompanied by Ta melts instability (balling) and accumulation of thermal stresses (tensile) in the adjacent solidified layers. The continuous partial relieving of these stresses and the balling phenomenon induced the formation of interconnected micropores, which resulted to pores-induced microcracks [40]. To fully understand the deepness and the geometry of the microgrooves formed during LPBF process, the cross-section of S-Ta2 was observed (Figure 13c). A semi-circular microgroove, which partially penetrated the strut connection was noticed (Figure 13d).

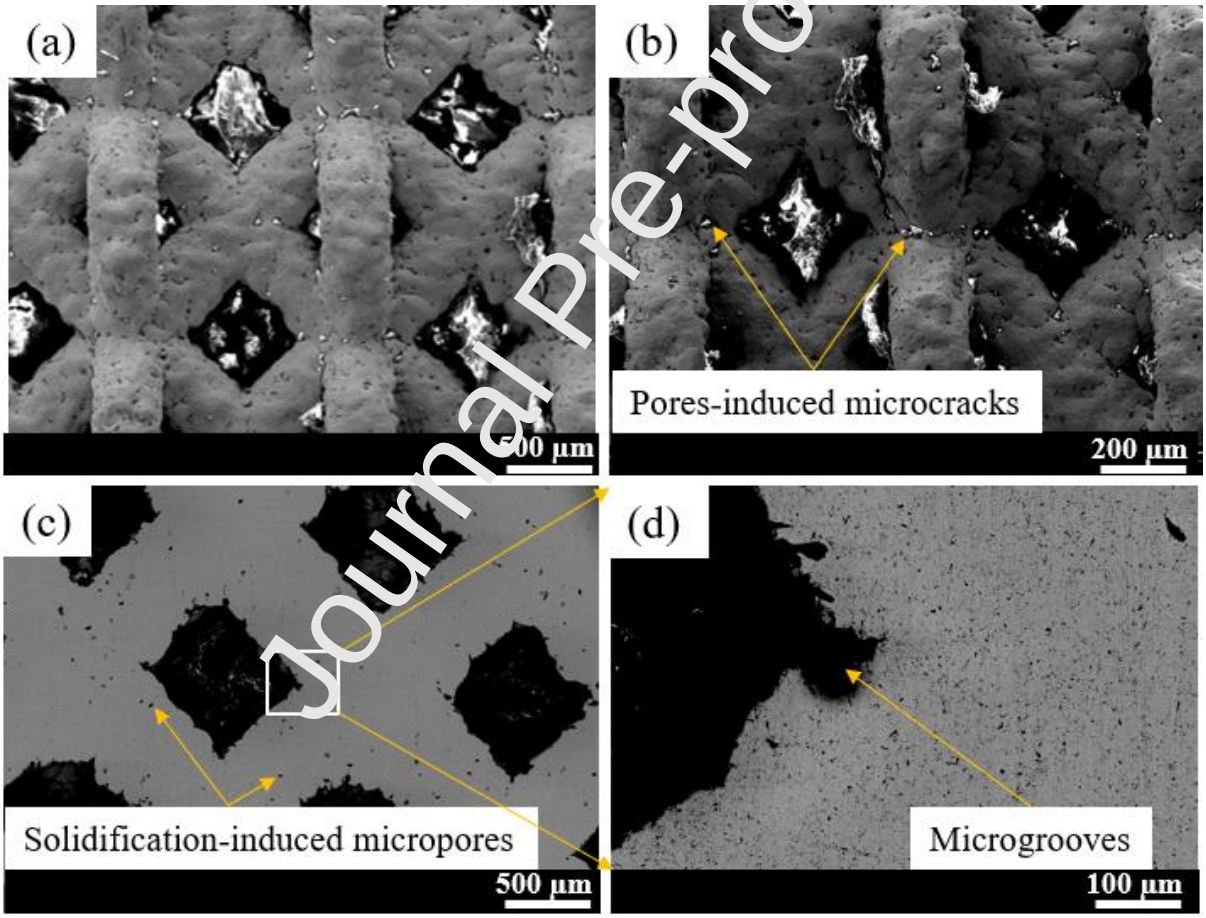

Figure 13 FESEM images of LPBF processed S-Ta2 specimen (a) surface morphology (b) pores-induced microcracks at struts connection (c) cross-sectional view of solidification-induced micropores and (d) microgrooves

3.4.3 Process-induced defects in Diamond truss scaffolds

The FESEM micrographs of S-Ta3 processed through parameter settings of 100 W laser power and 500 mm/s scanning speed is displayed in Figure 14. It is evident that various morphological features revealed the process-induced defects (Figure 14a). The pores-induced microcracks resulted from interconnected solidification-induced micropores and dislodge partially fused Ta powder are pronounced (Figure 14b). This might relate to low energy density used in fabricating this specimen. The partially fused Ta powder are more concentrated around the strut connection and edges (Figure 14c) and hence, the pores-induced microcracks are more pronounced in this region (Figure 14d). 3D printed nanostructured and micro scale porous scaffold surface was found to facilitate tissue growth and adhesion after implantation [41]. However, the undesired or undesigned features like process-induced defects degrades the properties of the LPBF-fabricated solid and porous scaffolds of Ta, thereby reducing its quality or service life.

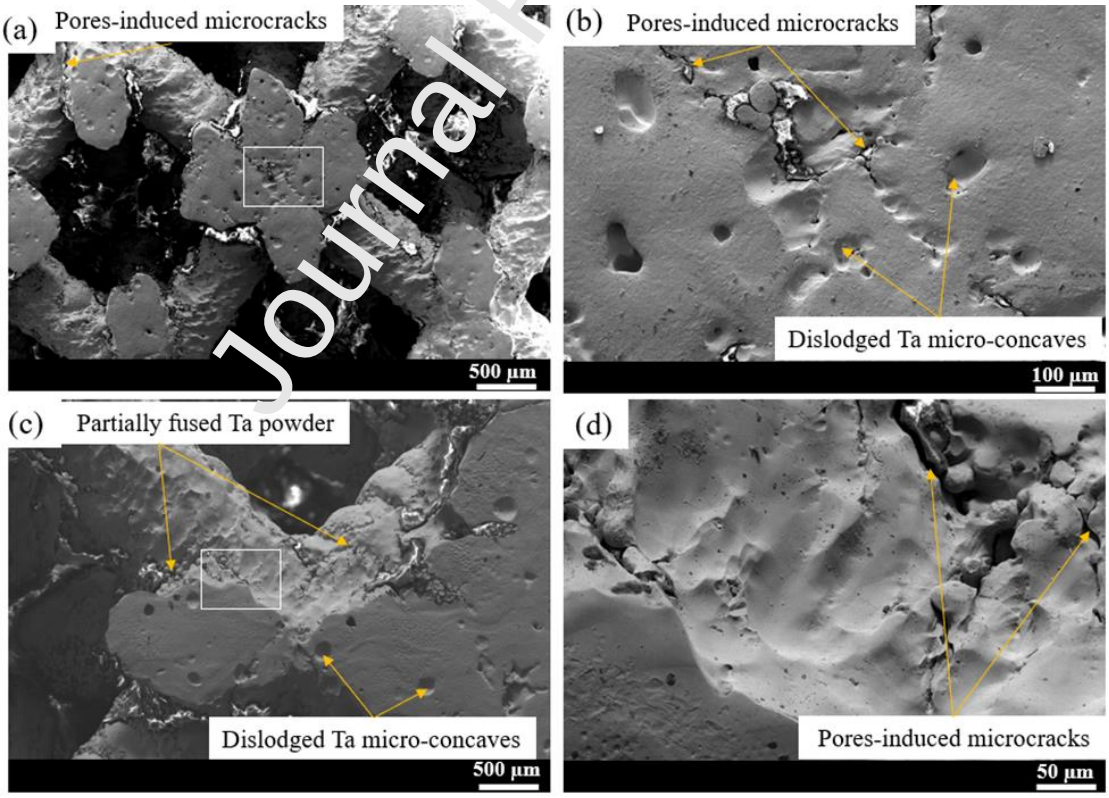

Figure 14 FESEM images of LPBF processed S-Ta3 specimen presenting various process-induced defects (a) pores-induced microcracks (b) pores-induced microcracks and micro-

concaves (c) partially fused Ta powder and (d) high magnification SEM image revealing the pores-induced microcracks.

3.5 Thermal-fluid flow simulation

Numerical simulation results for the two conditions are shown in Figure 15a-b. For the lower laser energy case in Figure15a, the conduction mode is observed since the laser power is not large and the scanning speed is relatively high. The powder bed surface is melted, but lack of fusion is observed in some places. Under the 250 W laser power and 100 mm/s scanning speed parameter conditions, a keyhole is formed due to its higher laser energy as shown in Figure 15b. Although, the scanning speed is slower in this case, the keyhole tip oscillates faster than the scanning speed scale in accordance with the unsteady melt pool motion, as shown in Figure 15c. The liquid/gas interface is drawn at one instant and cross-sectional shapes at three-time instants are superposed by the solid lines with the time interval of 3.5μs. The change in the keyhole surface shape induces the change in the laser ray absorption/reflection and thus induces the change in local heat distribution, which are all interconnected. The melt pool motion is affected by this heat change in a complicated way as well. The fast keyhole flapping motion occasionally leads to the micropores formation, as shown in Figure 15d. The observed porosity (the ratio of the pore volume to the melt pool volume) is 1.08 % at this instant. This porosity may vary temporarily, but the order of porosity is estimated around this value, which agrees with the present experimental observation. Therefore, the unsteady keyhole motion could be one reason for micropores formation. The interface between gas and liquid/solid is directly solved and the pores are identified as gas islands formed in the liquid metal. The pores here are generated due to the entrapment of the metal vapour at the keyhole tip, induced by the tip flapping motion. Although the porosity is not high or critical, suppression of this motion may require detailed thermal control, and further investigation is needed.

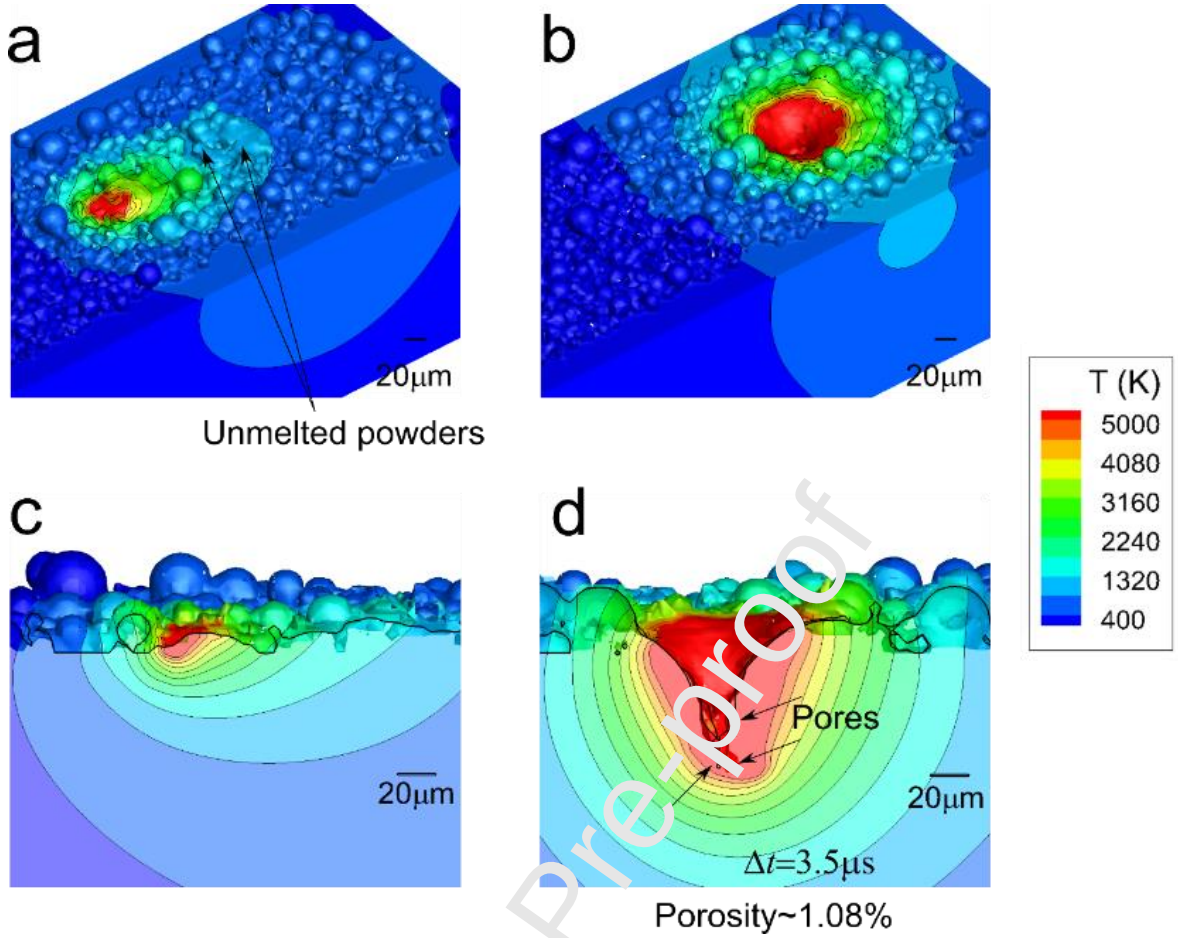

Figure 15 Simulation results (a) Low energy with laser power = 100W and scanning speed = 500 mm/s parameter conditions and (b) high energy with laser power = 250W and scanning speed = 100 mm/s parameter conditions (c) cross-section of "low energy" case where surface melting occurs in the conduction mode (d) cross-section of "high energy" case where the keyhole mode appears. The keyhole tip exhibits flapping motion and micropores are formed accordingly. The liquid/gas interface is drawn at one instant and cross-sectional shapes at three-time instants are superposed by the solid lines with the time interval of 3.5μs.

3.6 Vickers microhardness

The microhardness of LPBF processed solid and porous scaffolds of Ta is presented in Figure 16. The porous scaffolds processed through high energy with 250 W power and 100 mm/s scanning speed parameter settings has highest hardness value of 140 Hv while the lowest hardness of 131 Hv is observed in the solid Ta specimen processed through low energy with 100 W power and 500 mm/s scanning speed settings. This large variation in the hardness value

might relate to low energy of 6.7 J/mm^3 in the borderline setting. Microhardness of LPBF processed Ta was found to increase with increasing energy density. However, it decreases when too high energy density (362.32 J/mm^3) is used [22]. In a similar study, a higher hardness value of 228 Hv was reported, when processing trabecular Ta through LPBF technique [26]. LPBF processed Ta has a much higher hardness compared to those processed through conventional methods like casting, powder metallurgy and annealing with hardness of 110 Hv, 120 Hv and 90 Hv, respectively [42, 43].

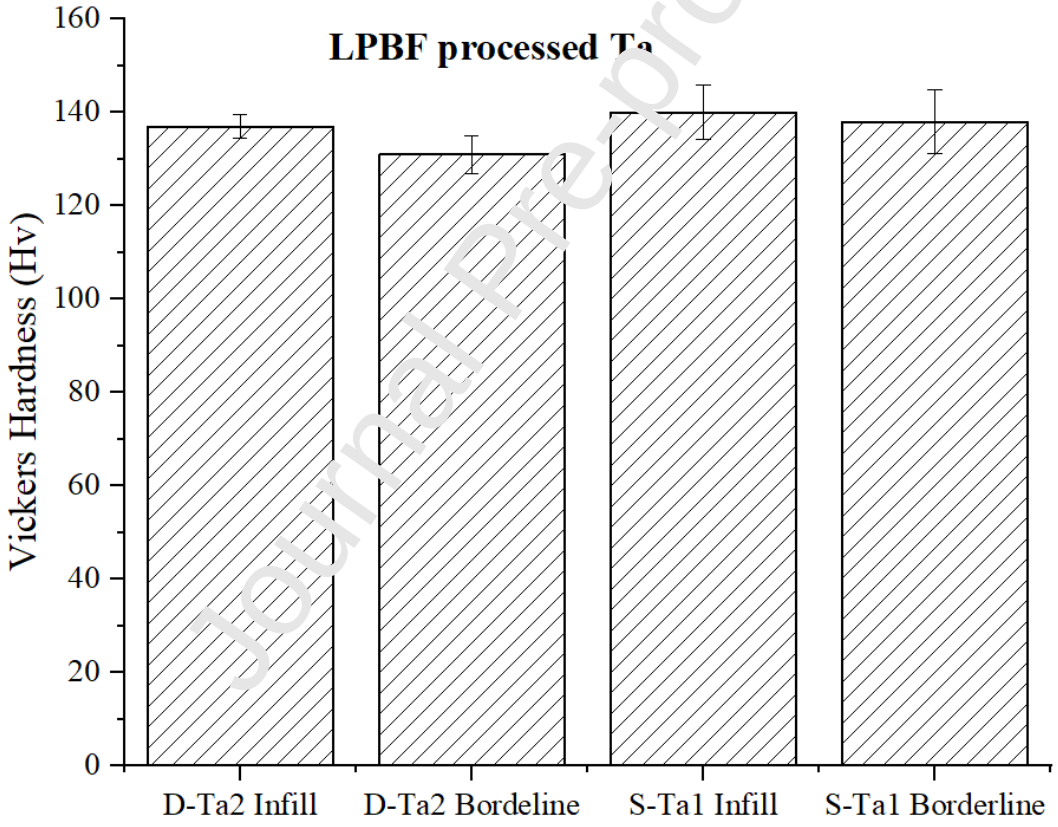

Figure 16 Vickers hardness of LPBF processed solid and porous scaffolds of Ta at low energy and high energyconditions with corresponding error bars.

4 Discussions

This study processed, characterized and assessed the microstructural features during LPBF of various solid and porous scaffolds of Ta, with emphasis on the types, distribution and formation mechanisms of microstructural deviations (process-induced defects). Process-induced defects degrade the mechanical and biomedical properties of the implants. Therefore, it needs to be highly minimized or eliminated.

4.1 Accuracy and density of LPBF processed Ta

The average standard deviation in the measured and designed dimensions along x, y and z directions of the cubic solid Ta specimens (D-Ta1, D-Ta2 and D-Ta3) were averagely calculated as ±0.0, ±0.02 and ±0.04, respectively (Table 4). This very low deviation confirmed the capability of the LPBF technique in fabricating highly dense pure Ta parts. Similarly, the standard deviation of the strut thickness for the porous scaffolds were calculated, with values 20.17, 7.89, 34.66 and 14.10 for the S-Ta1, S-Ta2, S-Ta3 and S-Ta4, respectively (Figure 3). This high discrepancy in the strut thickness of the designed and fabricated porous scaffolds of Ta might be related to the presence of unmelted and partially fused Ta powder, which led to a highly rough surface of the 3D printed porous Ta specimen. A similar finding was reported during the 3D printing of Ti-alloy porous scaffolds [44]. The high relative density of the cubic solid Ta specimens, D-Ta1 and D-Ta3 of 99.56 % and 99.43 %, respectively, confirmed the suitability of the LPBF technique to fabricate highly dense Ta parts. The low density (98.99 %) observed in the D-Ta2 specimen is believed to occur due to high micropores or partially fused Ta powder, owing to the low energy density used in processing this specimen. Other factors that might contribute to the decrease in density of the LPBF processed Ta is the increase in hatch distance and layer thickness, which resulted to a higher material overlap and hence, increasing the solidification-induced micropores [28].

4.2 Oxide formation and its effect on LFBF processed Ta

To reduce oxidation during the LPBF of Ta, high-purity (5 N purity with an oxygen level below 1.5 ppm) argon atmosphere was employed. However, the presence of secondary oxide, which is believed to be Ta_2O_5 and Ta_2O_3 were detected in the LPBF processed solid and porous scaffolds of Ta. The presence of oxygen was earlier detected by the EDX and XPS analysis, which chemically react with Ta to produce a secondary oxide. We have to state that, balling which resulted from oxidation during LPBF was not observed. Low level control of the oxygen content of non-spherical tantalum powder used for spheroidization is believed to enhance the purity and control the impurity content of the spherical Ta powder [45]. Nanoscale oxides are apatite formers. They are beneficial to the implants by enhancing not only the bone-implant bonding, but also its biocompatibility and resistance to corrosion [46, 47].

4.3 Phases formation during LPBF of Ta

The XRD patterns of LPBF processed Ta revealed various sharp and long peaks, which corresponds to BCC Ta. Obviously, the BBC Ta diffraction angles increased with increasing energy density. Other factors that might contribute to the shift of diffraction angles to higher values is high residual stress, which resulted in microscopic volume expansion and hence, affect the lattice structure of the Ta specimens [48]. Despite high residual stresses developed during LPBF, it does not always affect the diffraction angle [49]. Thus, our findings show no significant shift in the angle of diffraction in both infill and borderline parameter conditions. Our results are in agreement with the findings reported by Zhou, et al. [22]. At infill parameter conditions, whereby the scanning speed is low and the input energy is relatively high, the temperature rises, which resulted in thermal accumulation in the Ta molten pool. Heat release by conduction through the LPBF processed Ta decreases the residual stress. Thus, widen the diffraction angle of the BCC Ta and form a refined microstructure.

4.4 Microstructure and defects formation during LPBF of Ta

It is apparent that, columnar and equiaxed grains are formed in the LPBF processed Ta microstructures, as observed in Figure 8. In most situation, the orientation of the columnar grains occurred parallel to the building direction due to thermal gradient in the pool boundaries at the liquid/solid interface [50]. However, sometimes the local variations in heat transfer resulted in an inclination between the building and growth directions, which causes the columnar grains to grow in a different direction. Formation of equiaxed and fine grains is beneficial to LPBF processed Ta by enhancing its ductility (elastic limit) and biomedical properties [51]. Previous report revealed that, columnar grains can be completely eliminated through heat treatment [23].

The FESEM microstructural analysis of both solid and porous scaffolds of Ta processed through borderline and infill process parameter conditions revealed numerous process-induced defects. The microstructural defects observed include pores-induced microcracks, solidification-induced micropores, solidification-induced microcracks, micro-concaves and microgrooves. Unlike structural or designed pores, solidification-induced micropores are unintentional or undesigned micropores, which commonly occur in the LPBF processed part, due to vaporization of gasses. During the heating, melting and deposition of the top layer, the previous solidified layer will also be slowly heated. As the top layer cools rapidly, the shrinkage of such layer is hindered by the previous layer, which resulted in a thermal mismatch and hence, residual stresses are generated. Subsequent relieving of the already accumulated residual stresses causes solidification-induced microcracks [33]. The 100 W laser power and 500 mm/s scanning speed parameters combination in the borderline parameter settings implies very low laser energy (6.7 J/mm^3), which is insufficient to completely melt the Ta powder during the LPBF process. Postprocessing through conventional grinding/polishing dislodge the unmelted

or partially fuse Ta powder, which resulted to microgrooves and micro-concaves [52]. In the infill parameter settings, the laser power (250 W) and the scanning speed (100 mm/s) combination resulted to a high energy density. At this condition, Ta powder are highly melted. However, too high energy resulted in the instability of the melt pool, which causes a phenomenon called balling and the formation of interconnected porosities (pores-induced microcracks) (Figure 10) [40]. Process-induced defects have to be minimized or completely avoided to reduce their detrimental effect on the biomedical and mechanical properties of the LPBF built parts, thereby enhancing the performance of the fabricated parts [53]. Proper process parameter settings and optimization is proposed as the best approach to minimize the process-induced defects during LPBF [54].

4.5 Solidification-induced pores distribution and microhardness

The percentage area distribution of the porosities formed in the fabricated cubic solid D-Ta2 specimen was determined through particle analyser commend. The measured pore distribution of 1.19 % agrees with the simulated results, which has a volumetric pores distribution of 1.08 %. In a similar study, Ghods, et al. [55] investigated the role of re-used Ti-6Al-4V powder on the porosities and spatial distribution during the additive manufacturing of Ti-6Al-4V material. The average volumetric pore distribution of the 3D printed specimens was found to be 0.1±0.02%. The numerical simulation analysing the Ta molten pool behaviour and the pore formation mechanism contributes to the better understanding of the process parameters and hence, directed for optimisation in the future.

The microhardness results achieved show that, the specimens processed via low energy settings has lower hardness. This is caused by grain coarsening due to low density coupled with a very high speed (500 mm/s) [22]. On the other hand, the high hardness of the LPBF processed Ta is caused by grain refining, which strengthened the specimen's surface [56]. Additionally, the

rapid laser solidification resulted in a high accumulation of residual stresses during LPBF, which in-turn enhance surface hardness [57]. It has to be noted that, the high hardness-value of 3D printed Ta trabecular (228 Hv) reported by Yang, et al. [26] was achieved after postprocessing (annealing), which is believed to greatly raised its hardness. The as-built Ta has hardness-value of 190 Hv. However, this value is still higher than the hardness reported in this study. The relatively low hardness achieved in this study, might relate to presence of oxygen, which resulted in the formation of thin oxide films on the LPFB processed Ta surface. It is obvious that, oxide films like Ta_2O_5 and Ta_2O_3 reduces the hardness of metallic alloys [19].

5 Conclusion

Additive manufacturing of pure tantalum has been presented to understand the microstructure of the solid and porous scaffolds and to evaluate the process-induced defects for biomedical applications. The following specific conclusion can be drawn:

(1) The processability, microstructure, defect formation and generation mechanism, types and geometrical distribution of microstructural defects and the dimensional accuracies of the solid and porous scaffolds of Ta were successfully studied.

(2) The microstructure revealed the formation of nanostructures with roughness between 3.88 nm to 10.40 nm and a BBC Ta phase consisting of columnar, equiaxed and fine grains. Most of the specimens contained a short secondary oxide peak.

(3) Numerous undesired micro features such as solidification-induced micropores, pores-induced and solidification-induced microcracks, as well micro-concave and microgrooves, resulted from dislodged partially fuse Ta powder were assessed.

(4) The process-induced defects are denser and more prevalent on the solid and porous Ta specimens processed through borderline parameter settings. However, solidification-

induced micropores are predominant on the specimens processed through infill parameter conditions.

(5) Porous scaffolds of Ta processed through infill parameter settings were found to have maximum microhardness while the lower hardness value is observed in the solid Ta processed via borderline parameter settings.

(6) The numerical simulation conducted to study the formation and defect generation mechanism as well as the volumetric distribution of the porosities developed during the LPBF of Ta agrees with the experimental results. This demonstrates that, the model can predict and rationalise the process-induced porosity and gain insight into process improvement.

Acknowledgments

The research was funded and supported by the 90th Anniversary of Chulalongkorn University Fund (Ratchadaphiseksomphot Endowment Fund), Chulalongkorn University, Bangkok, Thailand. PP was supported by the Ratchadaphiseksomphot Endowment Fund of Chulalongkorn University (RES560530156-HR) and the Research Chair Grant 2012, the National Science and Technology Development Agency (NSTDA). We also acknowledge the support by the Second Century Fund (C2F), Chulalongkorn University, Bangkok, Thailand and Chulalongkorn Academic Advancement into its 2nd Century Project, Phase 2, Chulalongkorn University, Bangkok, Thailand. Chinnapat Panwisawas would like to acknowledge the funding from Innovation Fellowship by Engineering and Physical Science Research Council (EPSRC), UK Research and Innovation (UKRI) (grant number: EP/S000828/2).

References

[1] T. Hanawa, "Research and development of metals for medical devices based on clinical needs," *Science and technology of advanced materials,* 2012.

[2] R. C. Robertson, "Repair of cranial defects with tantalum," *Journal of Neurosurgery,* vol. 1, no. 4, pp. 227-236, 1944.

[3] J. Black, "Biologic performance of tantalum," *Clinical materials,* vol. 16, no. 3, pp. 167-173, 1994.

[4] R. C. Robertson and W. G. Peacher, "The use of tantalum foil in the subdural space," *Journal of Neurosurgery,* vol. 2, no. 4, pp. 281-284, 1945.

[5] B. H. Sagherian and R. J. Claridge, "The use of tantalum metal in foot and ankle surgery," *Orthopedic Clinics,* vol. 50, no. 1, pp. 119-129, 2019.

[6] Y. Liu, C. Bao, D. Wismeijer, and G. Wu, "The physicochemical/biological properties of porous tantalum and the potential surface modification techniques to improve its clinical application in dental implantology," *Materials Science and Engineering: C,* vol. 49, pp. 323-329, 2015.

[7] M. Weinmann, C. Schnitter, M. Stenzel, J. Markhoff, C. Schulze, and R. Bader, "Development of bio-compatible refractory Ti/Nb (/Ta) alloys for application in patient-specific orthopaedic implants," *International Journal of Refractory Metals and Hard Materials,* vol. 75, pp. 126-136, 2018.

[8] H. Matsuno, A. Yokoyama, F. Watari, M. Uo, and T. Kawasaki, "Biocompatibility and osteogenesis of refractory metal implants, titanium, hafnium, niobium, tantalum and rhenium," *Biomaterials,* vol. 22, no. 11, pp. 1253-1262, 2001.

[9] D. M. Findlay, K. Welldon, G. J. Atkins, D. W. Howie, A. C. Zannettino, and D. Bobyn, "The proliferation and phenotypic expression of human osteoblasts on tantalum metal," *Biomaterials,* vol. 25, no. 12, pp. 2215-2227, 2004.

[10] M. F. Meijer *et al.*, "Tibial component with and without stem extension in a trabecular metal cone construct," *Knee surgery, sports traumatology, arthroscopy,* vol. 25, no. 11, pp. 3644-3652, 2017.

[11] V. K. Balla, S. Bose, N. M. Davies, and A. Bandyopadhyay, "Tantalum—A bioactive metal for implants," *Jom,* vol. 62, no. 7, pp. 61-64, 2010.

[12] C. Dong, X. Bi, J. Yu, R. Liu, and Q. Zhang, "Microstructural evolution and sintering kinetics during spark plasma sintering of pure tantalum powder," *Journal of Alloys and Compounds,* vol. 781, pp. 84-92, 2019.

[13] E. Hosseini and M. Kazeminezhad, "Dislocation structure and strength evolution of heavily deformed tantalum," *International Journal of Refractory Metals and Hard Materials,* vol. 27, no. 3, pp. 605-610, 2009.

[14] C. Sungail and A. Abid, "Spherical tantalum feed powder for metal additive manufacturing," *Metal powder report,* vol. 73, no. 6, pp. 316-318, 2018.

[15] R. Wauthle *et al.*, "Additively manufactured porous tantalum implants," *Acta biomaterialia,* vol. 14, pp. 217-225, 2015.

[16] L. Thijs, M. L. M. Sistiaga, R. Wauthle, Q. Xie, J.-P. Kruth, and J. Van Humbeeck, "Strong morphological and crystallographic texture and resulting yield strength anisotropy in selective laser melted tantalum," *Acta Materialia,* vol. 61, no. 12, pp. 4657-4668, 2013.

[17] Q. Qin *et al.*, "3D printing of tantalum parts based on low molecular mass organic gel system," *International Journal of Refractory Metals and Hard Materials,* vol. 84, p. 105014, 2019.

[18] A. Bandyopadhyay, I. Mitra, A. Shivaram, N. Dasgupta, and S. Bose, "Direct comparison of additively manufactured porous titanium and tantalum implants towards in vivo osseointegration," *Additive manufacturing,* vol. 28, pp. 259-266, 2019.

[19] C. Sungail and A. D. Abid, "Additive manufacturing of tantalum–A study of chemical and physical properties of printed tantalum," *Metal Powder Report,* vol. 75, no. 1, pp. 28-33, 2020.

[20] N. Sri-utenchai, N. Pengrung, K. SrikonKorn, C. Puncreobutr, B. Lohwongwatana, and P. Sangasoongsong, "Using 3D Printing Technology for Corrective Biplanar Chevron Osteotomy with Customized Osteotomy Guide and Patient-Matched Monoblock Crosslink Plate in Treatment of Cubitus Varus Deformity: A Case Report and Technical Note," 2020.

[21] T. Thomrungpiyathan, S. Luenam, B. Lohwongwatana, W. Sirichativapee, K. Nabudda, and C. Puncreobutr, "A custom-made distal humerus plate fabricated by selective laser melting," *Computer Methods in Biomechanics and Biomedical Engineering,* vol. 24, no. 6, pp. 585-596, 2021.

[22] L. Zhou, T. Yuan, R. Li, J. Tang, G. Wang, and K. Guo, "Selective laser melting of pure tantalum: Densification, microstructure and mechanical behaviors," *Materials Science and Engineering: A,* vol. 707, pp. 443-451, 2017.

[23] L. Zhou *et al.*, "Microstructure tailoring to enhance strength and ductility in pure tantalum processed by selective laser melting," *Materials Science and Engineering: A,* vol. 785, p. 139352, 2020.

[24] C. Chandhanayingyong, K. Srikong, C. Puncreobutr, B. Lohwongwatana, R. Phimolsarnti, and B. Chuckpaiwong, "Three-dimensional printed, proximal phalangeal prosthesis with metatarsophalangeal joint arthroplasty for the treatment of a giant cell tumor of the fifth toe: The first case report," *International Journal of Surgery Case Reports,* vol. 73, pp. 84-89, 2020.

[25] G. Zhao *et al.*, "Porous tantalum scaffold fabricated by gel casting based on 3D printing and electrolysis," *Materials Letters,* vol. 239, pp. 5-8, 2019.

[26] J. Yang *et al.*, "Additive manufacturing of trabecular tantalum scaffolds by laser powder bed fusion: Mechanical property evaluation and porous structure characterization," *Materials Characterization,* vol. 170, p. 110694, 2020.

[27] J. Yang *et al.*, "Static Compressive Behavior and Material Failure Mechanism of Trabecular Tantalum Scaffolds Fabricated by Laser Powder Bed Fusion-based Additive Manufacturing," *International Journal of Bioprinting,* vol. 8, no. 1, 2022.

[28] V. Livescu, C. M. Knapp, G. T. Gray III, R. M. Martinez, B. M. Morrow, and B. G. Ndefru, "Additively manufactured tantalum microstructures," *Materialia,* vol. 1, pp. 15-24, 2018.

[29] H. Qian, T. Lei, P. Lei, and Y. Hu, "Additively Manufactured Tantalum implants for repairing bone defects: a systematic review," *Tissue Engineering Part B: Reviews,* vol. 27, no. 2, pp. 166-180, 2021.

[30] H. Taheri, M. R. B. M. Shoaib, L. W. Koester, T. A. Bigelow, P. C. Collins, and L. J. Bond, "Powder-based additive manufacturing-a review of types of defects, generation mechanisms, detection, property evaluation and metrology," *International Journal of Additive and Subtractive Materials Manufacturing,* vol. 1, no. 2, pp. 172-209, 2017.

[31] T. Yamamoto, M. Hara, and Y. Hatano, "Effects of fabrication conditions on the microstructure, pore characteristics and gas retention of pure tungsten prepared by laser powder bed fusion," *International Journal of Refractory Metals and Hard Materials,* vol. 95, p. 105410, 2021.

[32] H. Gong, K. Rafi, H. Gu, G. J. Ram, T. Starr, and B. Stucker, "Influence of defects on mechanical properties of Ti–6Al–4 V components produced by selective laser melting and electron beam melting," *Materials & Design,* vol. 86, pp. 545-554, 2015.

[33] A. Sola and A. Nouri, "Microstructural porosity in additive manufacturing: The formation and detection of pores in metal parts fabricated by powder bed fusion," *Journal of Advanced Manufacturing and Processing,* vol. 1, no. 3, p. e10021, 2019.

[34] N. J. Harrison, I. Todd, and K. Mumtaz, "Reduction of micro-cracking in nickel superalloys processed by Selective Laser Melting: A fundamental alloy design approach," *Acta Materialia,* vol. 94, pp. 59-68, 2015.

[35] J. Shinjo and C. Panwisawas, "Digital materials design by thermal-fluid science for multi-metal additive manufacturing," *Acta Materialia,* vol. 210, p. 116825, 2021.

[36] R. Wauthlé, J.-P. Kruth, M. Montero Sistiaga, L. Thijs, and J. Van Humbeeck, "New opportunities for using tantalum for implants with additive manufacturing," *European Cells & Materials,* vol. 26, 2013.

[37] E. Seki *et al.*, "Effect of heat treatment on the microstructure and fatigue strength of CoCrMo alloys fabricated by selective laser melting," *Materials Letters,* vol. 245, pp. 53-56, 2019.

[38] A. Dewaele, M. Mezouar, N. Guignot, and P. Loubeyre, "High melting points of tantalum in a laser-heated diamond anvil cell," *Physical Review Letters,* vol. 104, no. 25, p. 255701, 2010.

[39] E. Yasa, J.-P. Kruth, and J. Deckers, "Manufacturing by combining selective laser melting and selective laser erosion/laser re-melting," *CIRP annals,* vol. 60, no. 1, pp. 263-266, 2011.

[40] X. Nong, X. Zhou, and Y. Ren, "Fabrication and characterization of Fe-based metallic glasses by selective laser melting," *Optics & Laser Technology,* vol. 109, pp. 20-26, 2019.

[41] Z. Wang *et al.*, "Analysis of factors influencing bone ingrowth into three-dimensional printed porous metal scaffolds: a review," *Journal of Alloys and Compounds,* vol. 717, pp. 271-285, 2017.

[42] V. K. Balla, S. Banerjee, S. Bose, and A. Bandyopadhyay, "Direct laser processing of a tantalum coating on titanium for bone replacement structures," *Acta biomaterialia,* vol. 6, no. 6, pp. 2329-2334, 2010.

[43] G. Marinelli, F. Martina, S. Ganguly, and S. Williams, "Microstructure, hardness and mechanical properties of two different unalloyed tantalum wires deposited via wire+ arc additive manufacture," *International Journal of Refractory Metals and Hard Materials,* vol. 83, p. 104974, 2019.

[44] Y. Zheng, Q. Han, J. Wang, D. Li, Z. Song, and J. Yu, "Promotion of osseointegration between implant and bone interface by titanium alloy porous scaffolds prepared by 3d printing," *ACS biomaterials science & engineering,* vol. 6, no. 9, pp. 5181-5190, 2020.

[45] Z. Jin, C. He, J. Fu, Q. Han, and Y. He, "Balancing the customization and standardization: exploration and layout surrounding the regulation of the growing field of 3D-printed medical devices in China," *Bio-design and Manufacturing,* pp. 1-27, 2022.

[46] M. R. S. N. HAZWANI, L. X. Lim, Z. Lockman, and H. Zuhailawati, "Fabrication of titanium-based alloys with bioactive surface oxide layer as biomedical implants: Opportunity and challenges," *Transactions of Nonferrous Metals Society of China,* vol. 32, no. 1, pp. 1-44, 2022.

[47] P. Grewe *et al.*, "Stents: material, surface texture and design, in theory and practice," *Minimally Invasive Therapy & Allied Technologies,* vol. 11, no. 4, pp. 157-163, 2002.

[48] J. Moyer and G. Ansell, "The volume expansion accompanying the martensite transformation in iron-carbon alloys," *Metallurgical Transactions A,* vol. 6, no. 9, pp. 1785-1791, 1975.

[49] D. Gu, Y.-C. Hagedorn, W. Meiners, K. Wissenbach, and R. Poprawe, "Nanocrystalline TiC reinforced Ti matrix bulk-form nanocomposites by Selective Laser Melting (SLM): Densification, growth mechanism and wear behavior," *Composites Science and Technology,* vol. 71, no. 13, pp. 1612-1620, 2011.

[50] B. E. Carroll, T. A. Palmer, and A. M. Beese, "Anisotropic tensile behavior of Ti–6Al–4V components fabricated with directed energy deposition additive manufacturing," *Acta Materialia,* vol. 87, pp. 309-320, 2015.

[51] Z. Zhao, J. Chen, H. Tan, G. Zhang, X. Lin, and W. Huang, "Achieving superior ductility for laser solid formed extra low interstitial Ti-6Al-4V titanium alloy through equiaxial alpha microstructure," *Scr. Mater.,* vol. 146, pp. 187-191, 2018.

[52] D. D. Gu, W. Meiners, K. Wissenbach, and R. Poprawe, "Laser additive manufacturing of metallic components: materials, processes and mechanisms," *International materials reviews,* vol. 57, no. 3, pp. 133-164, 2012.

[53] B. Zhang, Y. Li, and Q. Bai, "Defect formation mechanisms in selective laser melting: a review," *Chinese Journal of Mechanical Engineering,* vol. 30, no. 3, pp. 515-527, 2017.

[54] T. Gustmann *et al.*, "Influence of processing parameters on the fabrication of a Cu-Al-Ni-Mn shape-memory alloy by selective laser melting," *Additive Manufacturing,* vol. 11, pp. 23-31, 2016.

[55] S. Ghods *et al.*, "Electron Beam Additive Manufacturing of Ti6Al4V: Importance of powder reuse on metal porosity, pore size and spatial distribution," *Pore Size and Spatial Distribution,* 2020.

[56] Q. Li *et al.*, "A comprehensive study of tantalum powder preparation for additive manufacturing," *Applied Surface Science,* vol. 593, p. 153357, 2022.

[57] E. Santos, K. Osakada, M. Shiomi, Y. Kitamura, and F. Abe, "Microstructure and mechanical properties of pure titanium models fabricated by selective laser melting," *Proceedings of the institution of mechanical engineers, part c: journal of mechanical engineering science,* vol. 218, no. 7, pp. 711-719, 2004.

Abdul Azeez Abdu Aliyu: Conceptualization, Formal analysis, Roles/Writing - original draft, Investigation. **Kitti Poungsiri**: Data curation, Investigation. **Boonrat Lohwongwatana**: Funding acquisition, Validation, Supervision. **Chedtha Puncreobutr**: Methodology, Supervision, **Krittima Tumkanon**: Project administration. **Surasak Kuimalee**: Resources. **Junji Shinjo**: Software. **Roger C. Reed**: Visualization. **Chinnapat Panwisawas**: Writing - review & editing.

Declaration of interests

☒The authors declare that they have no known competing financial interests or personal relationships that could have appeared to influence the work reported in this paper.

☐The authors declare the following financial interests/personal relationships which may be considered as potential competing interests:

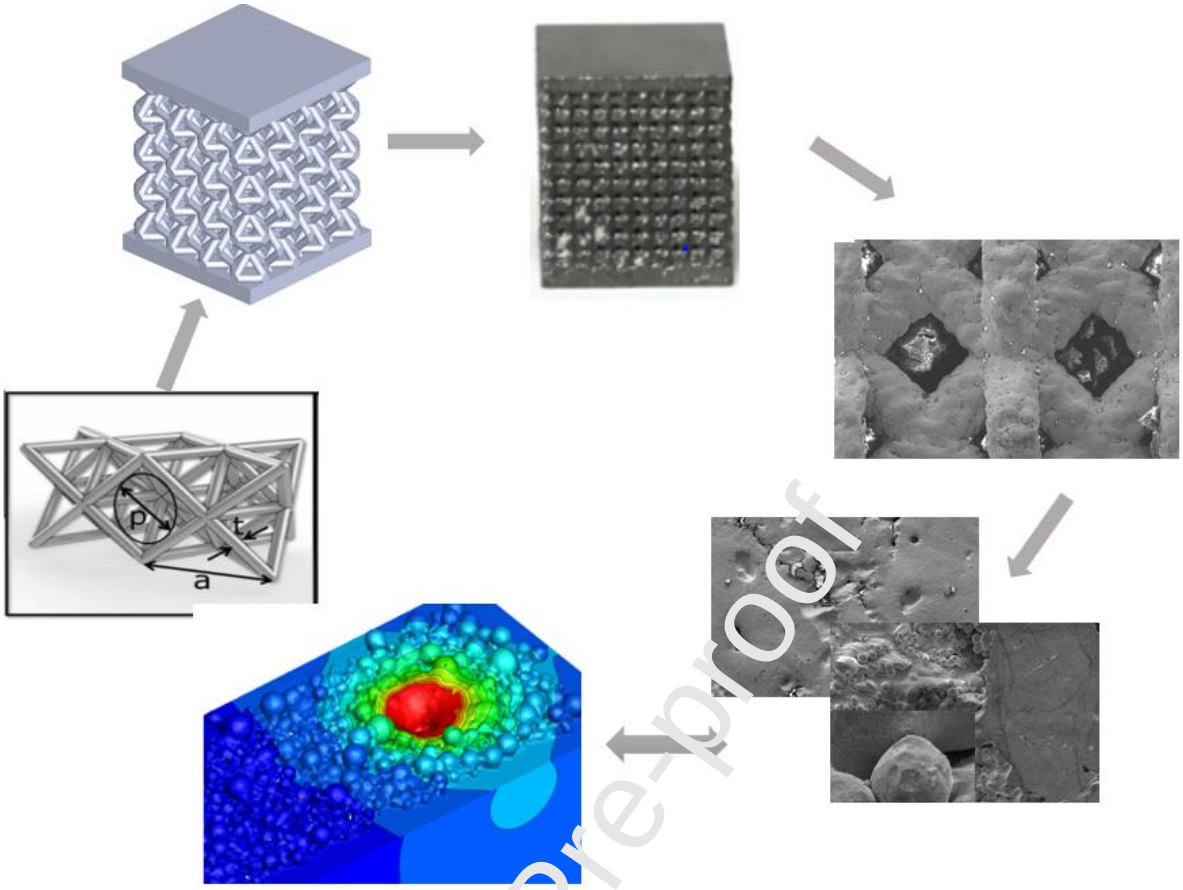

Highlights

- Highly dense and porous scaffolds of tantalum was successfully processed through laser powder-bed fusion process.
- The final microstructure of the laser powder-bed fusion processed tantalum contained equiaxed, columnar and fine grains.
- The formation mechanism of process-induced defects during laser powder-bed fusion of tantalum was assessed.
- Tantalum specimens processed through borderline parameter conditions have more process-induced defects.